

Globally Optimal Contour Deformations with Neural Networks

S. Jones,^a D. Maître,^{a,1} A. Olsson^a

^a*Institute for Particle Physics Phenomenology, Durham University, Durham DH1 3LE, UK*

E-mail: stephen.jones@durham.ac.uk, daniel.maitre@durham.ac.uk,
anton.olsson@durham.ac.uk

ABSTRACT:

In this article, we explore the use of contour deformation for the numerical evaluation of Feynman integrals after sector decomposition. In existing codes, the contour of integration is determined heuristically for each phase-space point by sampling the integrand. In this work, we introduce a method for choosing the contour deformation for an entire phase-space region using only an initial sampling or training step. We demonstrate that the resulting integrand has a lower variance than that obtained with heuristic methods and show that optimising a contour to reduce the estimated error of a Quasi-Monte Carlo sample is an ill-defined problem. The *a priori* knowledge of the integration path obtained in this work can be used to improve the speed of conventional integration methods or be leveraged for integration using neural networks, where, crucially, it removes the need to retrain the neural network for each phase-space point. The techniques described in this work can be adapted to other problems where a non-trivial integration path has to be chosen subject to a set of constraints.

¹Corresponding author.

Contents

| | | |
|----------|---|-----------|
| 1 | Introduction | 1 |
| 2 | Background | 3 |
| 2.1 | Contour deformation for Feynman integrals | 3 |
| 2.2 | Monte Carlo and Quasi-Monte Carlo integration | 7 |
| 2.3 | Numerical integration through a neural network | 8 |
| 2.4 | Selecting a contour deformation in pySECDEC | 9 |
| 2.5 | Physical thresholds and sector decomposition | 10 |
| 3 | Optimal contour equivalence | 12 |
| 4 | Network design and training | 14 |
| 4.1 | Guided deformation | 14 |
| 4.2 | Free deformation | 15 |
| 5 | One-loop bubble example | 16 |
| 5.1 | Free deformation | 18 |
| 6 | Two-loop box integral example | 21 |
| 6.1 | Results | 24 |
| 6.2 | Free deformation | 27 |
| 6.3 | Comparison with alternative neural network approach | 27 |
| 7 | Discussion | 29 |
| 8 | Conclusion | 31 |
| A | Analytical threshold derivation | 36 |
| B | Comparison of λ_i values | 36 |

1 Introduction

In perturbative approaches to Quantum Field Theories (QFTs) beyond tree-level, the precise definition of the theory requires a prescription for how the contour of integration should be chosen for loop integrals when singularities are encountered along the real axis of integration. The choice of contour is connected to preserving the causality of the theory, the

standard textbook approach is given by the Feynman $i\delta$ prescription. This prescription introduces a small imaginary part to each propagator of the theory in momentum space

$$P_i(q_i, m_i) = \frac{1}{q_i^2 - m_i^2 + i\delta}, \quad (1.1)$$

which defines the contour of integration. The loop integrals are then evaluated in the limit $\delta \rightarrow 0^+$.

After parameterising the loop integrals, e.g. using Schwinger or Feynman parameters, and performing the integration over the loop momenta, the Feynman $i\delta$ prescription manifests itself as a prescription for the contour of integration for the remaining parameter integrals; see, e.g. Ref. [1]. In fact, taking the prescription for the contour of integration in parameter space as a starting point can be advantageous for understanding causality and crossing symmetries of the scattering matrix [2]. From a practical viewpoint, the presence of singularities on the real axis of the integration parameters introduces an additional challenge in the evaluation of loop integrals. If we consider evaluating such loop integrals numerically, then naively we are forced to introduce an infinitesimal deformation which must then be extrapolated to zero, where the integrand may become singular within the integration domain. Methods for handling integrals with finite, non-zero δ and extracting the value in the infinitesimal limit have been employed successfully in various calculations [3–8].

In automated approaches to the direct integration of Feynman integrals, contour deformation is often the method of choice [9–19]. Using Cauchy’s theorem, the integration over the real line can be replaced by an appropriately chosen contour integral in the complex plane. It must be picked in accordance with the $i\delta$ prescription without crossing additional poles in the complex-plane [2, 19–31].

Although the procedure for finding a valid contour deformation, where it exists¹, is algorithmic, the resulting contours depend on a set of tunable deformation parameters, λ , (more generally functions) which must be chosen to obtain a valid contour and whose values can impact the variance of the resulting integrand. The challenge, therefore, is to pick values for these deformation parameters which both result in a valid contour and minimise the variance of the resulting integrand. In existing implementations of contour deformation, a pre-sampling and/or regression step is used to select valid values of the deformation parameters for each phase-space point (i.e. for each value of the kinematic invariants). The potential for improving the efficiency of the integration of contour-deformed Feynman integrals was explored in Ref. [33], where normalising flows were used to improve the variance of the integrand.

In this article, we present a method for obtaining valid values of the deformation parameters for a range of kinematic invariants, which also results in a low variance of the resulting integrand. This is achieved by training a neural network on the integrand both as a function of the Feynman parameters and the external kinematic invariants. The advantage of our approach is that the potentially expensive neural network training does not need to be repeated for each choice of kinematic parameters, and instead the trained network

¹The usual procedure for obtaining a contour can fail for integrals with a leading Landau singularity, see for example Ref [32].

can be used to obtain valid, low-variance contours for many phase-space points. We focus on integrands obtained using sector decomposition [34], as implemented in a variety of numerical packages [9–18].

Machine Learning has been used in other works to improve numerical integration [35–45], in these works, the integrand is considered fixed, and the sampling is adapted to improve the convergence of the numerical integration. The method described in this article can be applied to select an integration contour (and therefore fix the integrand) before using any of these integration improvement methods.

This article is structured as follows. In Section 2, we review the theoretical background. It is described how contour deformation is applied to parametric Feynman integrals, and we specify the type of deformations that are investigated. We also provide a brief summary of numerical integration techniques, including Quasi-Monte Carlo and neural network integration. Finally, we also describe how contour deformation is implemented in `pySECDEC` [9–15], a publicly available program for the evaluation of dimensionally regulated parameter integrals via sector decomposition, as well as how physical thresholds of individual sector integrals can move as a result of sector decomposition. In Section 3, we discuss the equivalence of optimal contours between networks trained globally and networks trained on individual phase-space points. Section 4 provides the details on the neural network architecture and how the training is performed. In Sections 5 and 6, the one-loop bubble and two-loop box integrals are considered as examples. In Section 7, we discuss the general results we obtained for the two previously mentioned examples. In Section 8, we summarise our main conclusions.

2 Background

We review the necessary background for computing Feynman Integrals in the Minkowski (physical) regime using Feynman parameters. In Section 2.1, we present an overview of the problem of selecting a contour of integration for Feynman integrals. In Section 2.2, we briefly summarise the key features of Monte Carlo and Quasi-Monte Carlo integration. In Section 2.3, we describe a method for computing integrals using a neural network to approximate the primitive. We recap the selection of the integration contour in the public `pySECDEC` package in Section 2.4. Finally, in Section 2.5, we highlight how the application of sector decomposition can complicate the threshold structure of the integrand.

2.1 Contour deformation for Feynman integrals

A general dimensionally regulated Feynman integral can be written in parametric form,

$$I(\mathbf{s}) = \frac{(-1)^\nu \Gamma(\nu - LD/2)}{\prod_{i=1}^{N+1} \Gamma(\nu_i)} \lim_{\delta \rightarrow 0^+} \int_{\mathbb{R}_{\geq 0}^{N+1}} \prod_{i=1}^{N+1} dx_i x_i^{\nu_i - 1} \frac{\mathcal{U}(\mathbf{x})^{\nu - (L+1)D/2}}{(\mathcal{F}(\mathbf{x}; \mathbf{s}) - i\delta)^{\nu - LD/2}} \delta(1 - \sum_i x_i), \quad (2.1)$$

where $\mathcal{U}(\mathbf{x})$ and $\mathcal{F}(\mathbf{x}; \mathbf{s})$ are the first and second Symanzik polynomials², $D = 4 - 2\epsilon$ are the number of space-time dimensions, ν_i are the powers of the Feynman propagators and $\nu = \sum_i \nu_i$. The $\mathcal{U}(\mathbf{x})$ and $\mathcal{F}(\mathbf{x}; \mathbf{s})$ polynomials are functions of the Feynman parameters, and $\mathcal{F}(\mathbf{x}; \mathbf{s})$ additionally depends on the kinematic invariants. The $\delta > 0$ is a prescription for the analytic continuation of special functions, such as logarithms, that appear in the integration result. Singularities originating from the integration boundaries cannot be resolved with contour deformation but can be extracted by applying a sector decomposition, which transforms the integral, $I(\mathbf{s})$, into a linear combination of sector integrals, $I_k(\mathbf{s})$, such that³,

$$I(\mathbf{s}) \rightarrow \sum_{k=0} c_k I_k(\mathbf{s}), \quad I_k(\mathbf{s}) = \int_0^1 dx_1 \cdots dx_N \frac{U_k(\mathbf{x})^a}{(F_k(\mathbf{x}; \mathbf{s}) - i\delta)^b}, \quad (2.2)$$

where the $U_k(\mathbf{x})$ and $F_k(\mathbf{x}; \mathbf{s})$ are the sector decomposed Symanzik polynomials in sector k ⁴, and the ϵ -structure has been factorised and absorbed into the coefficients c_k , together with all prefactors of Eq. (2.1), such that the sector integrals $I_k(\mathbf{s})$ have only integrable singularities and are suitable for numerical integration. Note that after sector decomposition, the integration domain has been remapped to the unit hypercube $[0, 1]^N$. Since the $F_k(\mathbf{x}; \mathbf{s})$ can still vanish within the integration domain, a contour deformation is required for numerical integration. A general contour deformation is constructed by shifting each integration variable by a small imaginary part,

$$x_i \rightarrow z_i = x_i + i\tau_i(\mathbf{x}; \mathbf{s}), \quad (2.3)$$

where τ is a real function vanishing at the boundary of the x hypercube. Provided the integration contour vanishes at the boundaries and does not enclose any poles nor cross any branch cuts, Cauchy's theorem can be applied to express a sector integral as,

$$I_k(\mathbf{s}) = \int_C dz_1 \cdots dz_N \frac{U_k^a(\mathbf{z})}{(F_k(\mathbf{z}; \mathbf{s}) - i\delta)^b} = \int_0^1 dx_1 \cdots dx_N \frac{U_k(\mathbf{z})^a}{(F_k(\mathbf{z}; \mathbf{s}) - i\delta)^b} \det \left(\frac{\partial \mathbf{z}}{\partial \mathbf{x}} \right), \quad (2.4)$$

where in the second equality we have remapped the integration variables back from the complex z_i to the real $x_i \in [0, 1]$.

The sign and magnitude of the deformations τ_i are important for the numerical efficiency of the integration. Too small a deformation leads to large peaks subject to large cancellations. Too large deformations can lead to the path crossing a pole or a branch cut, which yields the wrong result.

To develop an intuition for the choice of a good deformation, we examine a two-dimensional example $F_\delta = F(x_1, x_2) - i\delta$. The integrand has a pole where $F_\delta = F - i\delta = 0$.

²We use the symbols \mathbf{s} and \mathbf{x} to collect all kinematic invariants and integration parameters. Note that \mathbf{x} contains $N + 1$ elements before integration over the δ functional and N after its integration, while \mathbf{s} always contains M elements.

³There are also subtraction terms present that regulate the isolated endpoint divergences. These consist of integrands evaluated at 0 for some subset of the integration variables, and we suppress these terms for ease of notation.

⁴In the remainder of this paper, we will often drop the sector indices and consider a generic sector integral.

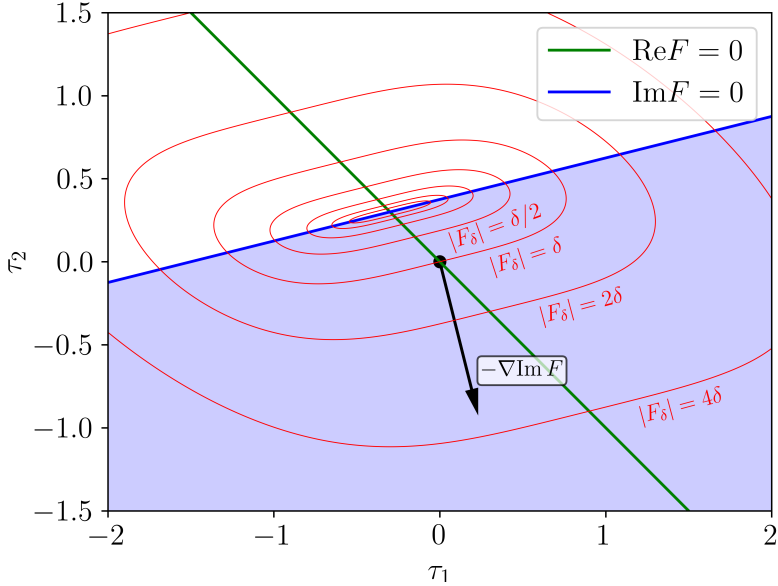


Figure 1. Plane spanned by the imaginary components of z_1 and z_2 at values of x_1 and x_2 such that $F(x_1, x_2) = 0$. We consider the first sector (red) in Section 2.5 with $\delta = 3/2$. We plot the value \dots . The green line and the blue line represent where the real and imaginary parts of $F_\delta = 0$. At $F_\delta = 0$ the integrand has a divergence. The red lines are contours of constant F_δ . With no deformation, the integration path is represented by the black dot. It is on the $\text{Re}F_\delta = 0$ by our choice of location for the real parts x_1, x_2 . As explained in the text, the best direction to deform to avoid the zero of F_δ for $\delta \rightarrow 0$ is in the inverse direction of the gradient of F , shown here with the black arrow.

We now fix the values of the real part x_1, x_2 of z_1, z_2 to a location where the unregulated, unshifted F polynomial vanishes, $F(x_1, x_2) = 0$, and consider the plane spanned by the imaginary parts $\text{Im}(z_1) = \tau_1$ and $\text{Im}(z_2) = \tau_2$. The undeformed path goes through the $\tau_1 = \tau_2 = 0$ point, at which the regulated F_δ polynomial has the value $F_\delta = -i\delta$.

When we shift the integration contour, we are moving the location of the intersection of this plane with the integration path from the origin to a different location. To maintain the same value of the integral, we have to do so without hitting a pole. The poles are located at the intersection of the $\text{Im}F_\delta = 0$ and the $\text{Re}F_\delta = 0$ surface. Since we know the original contour has $\text{Im}F_\delta = -\delta$ we can guarantee staying away from the poles by requiring that the imaginary part of F stays negative continuously as we deform the path. The safest direction to move into is the one that decreases the value of the imaginary part of F the most, that is, following the negative gradient of the imaginary part of F . If we expand F around $\tau_1 = 0$ and $\tau_2 = 0$ we obtain,

$$F(z_1, z_2) = F(x_1, x_2) + i\tau_1 \left. \frac{\partial F(z_1, z_2)}{\partial z_1} \right|_{\tau_1, \tau_2=0} + i\tau_2 \left. \frac{\partial F(z_1, z_2)}{\partial z_2} \right|_{\tau_1, \tau_2=0} + \mathcal{O}(\tau_1^2, \tau_2^2, \tau_1 \tau_2), \quad (2.5)$$

which means that by choosing,

$$\tau_1 \propto -\frac{\partial F(z_1, z_2)}{\partial z_1} \Big|_{\tau_1, \tau_2=0} \quad \text{and} \quad \tau_2 \propto -\frac{\partial F(z_1, z_2)}{\partial z_2} \Big|_{\tau_1, \tau_2=0}, \quad (2.6)$$

and keeping the deformation small enough, we can avoid moving the contour across a pole.

Note that the deformation is only required in the vicinity of locations where the real part of F vanishes. In practice, it is usually easier to define one continuous deformation along the entire integration range, even in regions where there is no risk of approaching a pole (actually introducing a deformation there creates this risk if the deformations are large enough).

We call the deformation defined by

$$z_i = x_i - i\lambda_i x_i (1 - x_i) \frac{\partial F(\mathbf{z})}{\partial z_i} \Big|_{\tau=0}, \quad (2.7)$$

a *guided deformation*. The only free parameters are the positive constants λ_i that are chosen such that the sign of the imaginary part of the F polynomial does not change. This is the type of deformation which is implemented in pySECDEC, where the λ_i are non-negative real numbers.

The first modification we investigate in this article is to promote the constant λ to a function of the physical parameters s_i and model this function with a neural network. The idea is to fit a function $\lambda(s_1, \dots, s_M)$ such that the variance of the integral is reduced and the sign of $\text{Im}(F)$ stays negative. The function for $\lambda(\mathbf{s})$ is implemented as a neural network (though it could be any other type of interpolating function) and trained to minimise the loss,

$$L = L_{\text{var}} + C \int d\mathbf{x} d\mathbf{s} \text{ReLU}(\text{Im}F(\mathbf{z}(\mathbf{x}; \mathbf{s}); \mathbf{s}))^2, \quad (2.8)$$

where L_{var} is described in Section 3, and the second term, containing the ReLu function function, $\text{ReLU}(x) = \max(x, 0)$, penalises choices of λ that lead to a wrong sign in the imaginary part of F . In practice, a large value of C and a safety margin ensure that the condition is imposed strictly.

The second modification we investigate is by introducing more flexibility to the deformation by promoting $\lambda(s_1, \dots, s_M) \rightarrow \lambda(x_1, \dots, x_N; s_1, \dots, s_M) = \lambda(\mathbf{x}; \mathbf{s})$. The function $\lambda(\mathbf{x}; \mathbf{s})$ is much more flexible than the fixed-lambda scheme $\lambda(\mathbf{s})$, and can negotiate situations where one would like a small λ to reduce the variance of the integrand in one part of the integration region, but a large value of λ to avoid large values of the integrand close to a pole.

We will use a neural network to find a suitable function $\lambda(x_1, \dots, x_N; s_1, \dots, s_M)$. The Jacobian of the transformation can easily be computed by taking the appropriate derivatives of the neural network. Our implementation could leverage the infrastructure developed in Ref. [46] to calculate these derivatives.

2.2 Monte Carlo and Quasi-Monte Carlo integration

The contour deformed sector integrals of Eq. (2.4) can be evaluated numerically with Monte Carlo (MC) methods. In classical MC integration, an estimate is computed as,

$$I[f] = \int_0^1 d\mathbf{x} f(\mathbf{x}) \approx \frac{1}{n} \sum_{i=0}^{n-1} f(x_{1,i}, \dots, x_{N,i}), \quad (2.9)$$

where $f(x_1, \dots, x_N)$ is the integrand and the $(x_{1,i}, \dots, x_{N,i})$ are n uniformly random sample points. The randomness of the samples allows an unbiased estimate of the variance of the integral I in terms of the variance of the integrand $\sigma(f)$,

$$\sigma^2(I) \approx \frac{\sigma^2(f)}{n} = \frac{I(f^2) - I(f)^2}{n}. \quad (2.10)$$

In pySECDEC the most performant integrators are instead based on Quasi-Monte Carlo (QMC) integration. The idea is to choose the n sample points deterministically from low-discrepancy sequences, since this bounds the integration error [47]. One way of achieving this is with a rank-1 shifted lattice rule, where the integral estimate is computed as [12],

$$I[f] \approx \bar{Q}_{n,m}[f] \equiv \frac{1}{m} \sum_{k=0}^{m-1} Q_n^{(k)}[f], \quad Q_n^{(k)}[f] \equiv \frac{1}{n} \sum_{i=0}^{n-1} f\left(\left\{\frac{i\mathbf{w}}{n} + \Delta_k\right\}\right), \quad (2.11)$$

where Δ_k are shift vectors, $\mathbf{w} \in \mathbb{Z}^N$ is a generating vector with elements coprime to n , and the curly brackets indicate taking the fractional part of each component of the vector inside. The elements of Δ_k are random numbers, which allows for an unbiased error to be estimated as [12]

$$\sigma_{n,m}^2[f] \approx \frac{1}{m(m-1)} \sum_{k=0}^{m-1} (Q_n^{(k)}[f] - \bar{Q}_{n,m}[f])^2. \quad (2.12)$$

In practice, only around 10–20 random shifts are necessary to obtain a reliable estimate [12].

An improvement to the QMC quadrature rule in Eq. (2.11) is the median lattice construction [15, 48]. It is motivated by the observation that lattices constructed from generating vectors with elements chosen from the set $\{1 \leq w \leq n-1 \mid \gcd(w, n) = 1\}$ are often good choices, but are known to sometimes lead to so-called unlucky lattices. These are lattices that randomly lead to a much worse error estimate than other lattices of similar size. It has been shown that picking lattices based on $\text{median}(Q_{n,\mathbf{w}_1}[f], \dots, Q_{n,\mathbf{w}_r}[f])$, where each estimate $Q_{n,\mathbf{w}_i}[f]$ is constructed from a unique generating vector \mathbf{w}_i , substantially alleviates this problem, while preserving the convergence rate of the default rule. In practice, selecting the median lattice based on ~ 13 estimates tends to lead to good performance [15]. In this paper, we use QMC integration based on median lattice rules to benchmark our choices of contour deformations for sector decomposed Feynman integrals.

QMC integration works best for integrands that belong to certain weighted function spaces, such as the Korobov function space for periodic and α times differentiable functions. For such integrands, it can be shown that the worst-case error converges close to $\mathcal{O}(n^{-\alpha})$ [12]. Our sector decomposed integrands are typically smooth but, in general, not

periodic. They can be periodized by applying a Korobov transformation. This transformation is defined through a reparametrisation of the integration variables specified through a suitably normalised weight function,

$$\omega = At^\alpha(1-t)^\beta, \quad \int_0^1 dt \omega(t) = 1, \quad (2.13)$$

where α and β are parameters of the transformation and A is a normalisation constant. The precise variable transformation is then given by

$$x(t) = \int_0^t dt' \omega(t'). \quad (2.14)$$

Inserting into the integral definition, we obtain

$$\int_0^1 dx f(x) = \int_0^1 dt \omega(t) f(x(t)). \quad (2.15)$$

For the work presented in this article, unless otherwise specified, we use the weight function and transformation obtained by setting $\alpha = \beta = 3$, namely,

$$\omega(t) = 140t^3(1-t)^3, \quad x = t^4(35 - 84t + 70t^2 - 20t^3) \quad (2.16)$$

for each of the x_i variables. This choice makes the integrand vanish at the x_i boundaries.

2.3 Numerical integration through a neural network

Another integration strategy is that explored in Ref. [46], where the idea is to fit a neural network such that its derivative matches the integrand, so that the undifferentiated neural network is a fit to the primitive of the integrand. This yields a simple evaluation of the integral as a combination of the primitive approximation evaluated at the boundaries of integration. We target contour deformed sector integrals as in Eq. (2.4), which we can write in the form,

$$I_\mu(s_1, \dots, s_M) = \int_0^1 dx_1 \cdots dx_N f_\mu(x_1, \dots, x_N; s_1, \dots, s_M), \quad (2.17)$$

where μ enumerates components of the integrand, such as real and imaginary parts, or related sector integrands. We use a neural network

$$\mathcal{N}_\mu(x_1, \dots, x_N; s_1, \dots, s_M) \quad (2.18)$$

which takes $N + M$ input parameters and has as one output node for each component of I_μ . The neural network is trained to minimise the loss,

$$L(x_1, \dots, x_N; s_1, \dots, s_M) = \sum_\mu \text{MSE} \left(f_\mu(x_1, \dots, x_N; s_1, \dots, s_M), \frac{d\mathcal{N}_\mu(x_1, \dots, x_N; s_1, \dots, s_M)}{dx_1 \cdots dx_N} \right), \quad (2.19)$$

where MSE is the mean squared error. In the case where f is complex, \mathcal{N} has two components, one for the real and one for the imaginary part, and the loss is the mean modulus of

the difference between the complex integrand and the complex derivative of the network. After training, we obtain our estimate for the value of the integral as,

$$I_\mu(s_1, \dots, s_M) \simeq \mathcal{I}_\mu(s_1, \dots, s_M) = \sum_{b_1, \dots, b_n=0,1} (-1)^{n-\sum b_i} \mathcal{N}_\mu(b_1, \dots, b_N; s_1, \dots, s_M). \quad (2.20)$$

For this method to work for integrands necessitating a contour deformation, the form of the deformation has to be a known function of the physical parameters, s_i . It cannot, for example, be defined as a phase-space dependent iterative process. The deformations we introduce in this article satisfy this requirement.

2.4 Selecting a contour deformation in pySECDEC

The integration and contour deformation procedures described in Sections 2.1–2.3 can be directly applied to finite Feynman integrals. In practice, we find that the variance of finite integrals (after a change of variables to remove integrable singularities) is usually very high. For this reason, we prefer to consider sector-decomposed integrals. As a consequence of this, we can also apply all of these techniques to divergent integrals.

pySECDEC is a program for the numerical integration of dimensionally regulated parameter integrals. It implements various sector decomposition routines, which cast Feynman integrals in the form of Eq. (2.2). It can obtain numerical results in the Minkowski regime by implementing a contour deformation. The deformation is defined as in Eq. (2.7) and currently the λ_i are initialised based on the heuristic choice,

$$\lambda_i = \min \left(\left| x_i (1 - x_i) \frac{\partial F(\mathbf{x})}{\partial x_i} \right|^{-1} \right) \quad (2.21)$$

estimated using a set of presamples [33]. If the initial values are such that either the sign is wrong or the contour encloses poles, all λ_i are iteratively reduced by a factor of 0.9 until a valid deformation is found. Additionally, pySECDEC enforces $\lambda_i \in (10^{-6}, 1)$ to avoid numerical instabilities. While this approach works quite well in practice, there are several reasons why this might not lead to the optimal contour:

- not all λ_i need to be reduced if the contour is not valid, reducing it along only one coordinate might be sufficient.
- the procedure starts with values of λ_i that are close to the largest values thought empirically valid, but it is not always the case that the largest deformations lead to lower variance. Indeed, in some cases, no deformation at all is best, and the above procedure would not necessarily detect it.

Moreover, pySECDEC recycles no knowledge of what good choices for the λ_i are between integrations for different phase-space points. The integration wastes time evaluating presamples if the initial values are far away from producing a valid contour. The efficiency of pySECDEC would therefore be improved if the presampling step could be replaced by a function that immediately provides a set of valid λ_i that integrate efficiently.

With these motivations in mind, we have extended the DISTEVAL integrator in pySECDEC to accept user-defined starting values for the deformation parameters. If the specified values are found to produce an invalid contour, they will be decreased iteratively as described above, which means bad choices still produce correct results. The user-defined λ_i are, however, not limited to the range $(10^{-6}, 1)$.

The feature is implemented as an input argument `initial_deformation_parameters` that accepts a dictionary of tuples of lists, where each entry is on the form `(<name>_integral, <sector_name>): [λ₁, ..., λₙ]`. The `<name>` is a string specified in the generation file, and is the name of the pySECDEC output directory, and `<sector_name>` is a string of the form `sector_k_order_i` where `k` is the sector index and `i` is the order in the ϵ expansion (`n` is used to denote negative numbers). The names of all sectors can be found in the `<name>/disteval/<name>_integral.json` file in the pySECDEC output directory. It is possible to specify deformation parameters for a subset of the sectors. In that case, any sectors left out will have the λ_i determined by the presampling procedure described above. The feature will be made available in the next public release of pySECDEC, which also includes an example input file for the `box1L` integral.

2.5 Physical thresholds and sector decomposition

The physical thresholds of a Feynman integral can appear at non-physical values of the kinematics in the sectors of a sector decomposition. This behaviour can complicate the optimisation of the contour deformation for a region of phase-space, as, after sector decomposition, the integrand can develop an imaginary part and/or discontinuities in its derivatives at values of the kinematic invariants that do not correspond to physical thresholds. Furthermore, this behaviour can differ for each sector of the integral, meaning that the phase-space region for which a contour is optimal can differ for each sector.

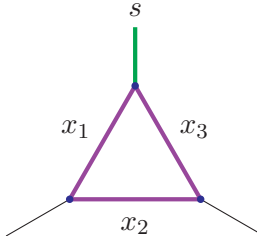


Figure 2. One-loop massive triangle integral.

To understand this effect, let us consider the sector decomposition of a one-loop triangle integral with three massive propagators, depicted in Figure 2,

$$\mathcal{I}(\mathbf{s}) = -\Gamma(1 + \epsilon) \int_{\mathbb{R}_{\geq 0}^3} dx_1 dx_2 dx_3 \frac{\mathcal{U}(\mathbf{x})^{-1+2\epsilon}}{(\mathcal{F}(\mathbf{x}; \mathbf{s}) - i\delta)^{1+\epsilon}} \delta(1 - x_3). \quad (2.22)$$

The Symanzik polynomials are given by,

$$\mathcal{U}(\mathbf{x}) = x_1 + x_2 + x_3, \quad (2.23)$$

$$\mathcal{F}(\mathbf{x}; \mathbf{s}) = -sx_1x_3 + m^2(x_1 + x_2 + x_3)^2. \quad (2.24)$$

Here, m is the mass of the internal propagator and $p^2 = s$ is a Mandelstam invariant corresponding to the off-shellness of one external leg.

The physical thresholds of a Feynman integral are encoded in the variety defined by $\mathcal{F}(\mathbf{x}; \mathbf{s}) = 0$ (i.e. the zero-locus of $\mathcal{F}(\mathbf{x}; \mathbf{s})$). Factoring out the squared mass, m^2 , we can write,

$$\tilde{\mathcal{F}}(\mathbf{x}; \mathbf{s}) = -\tilde{s}x_1x_3 + (x_1 + x_2 + x_3)^2, \quad (2.25)$$

with $\tilde{s} = s/m^2$. Integrating over x_3 using the delta-functional in Eq. (2.22) and solving $\tilde{\mathcal{F}}(\mathbf{x}; \mathbf{s}) = 0$ for \tilde{s} we obtain,

$$\tilde{s} = x_1^{-1}(1 + x_1 + x_2)^2. \quad (2.26)$$

Examining this solution, we find that the minimum non-negative value of \tilde{s} for which we can encounter a zero of $\tilde{\mathcal{F}}(\mathbf{x}; \mathbf{s})$ in the non-negative octant of \mathbf{x} is $\tilde{s} = 4$, which is obtained for $x_1 = 1, x_2 = 0$. The value $\tilde{s} = 4$ corresponds to the physical threshold at which the propagating particles with associated Feynman parameters x_1 and x_3 are on-shell.

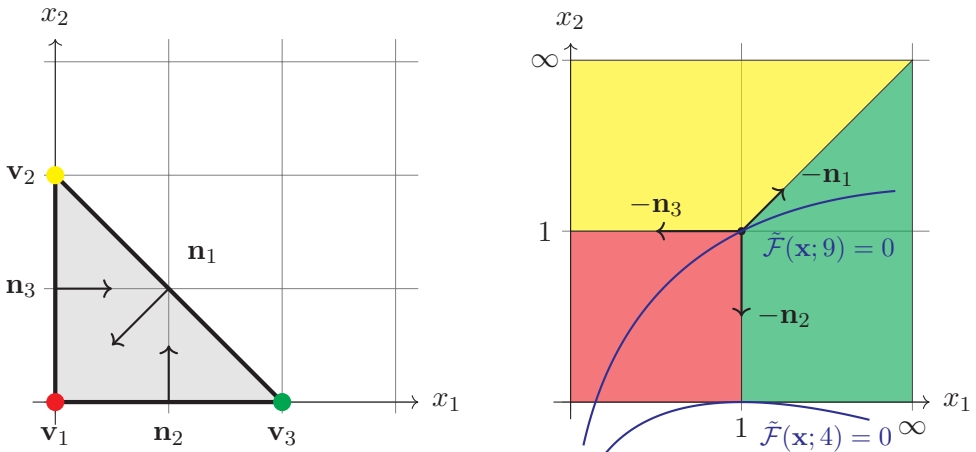


Figure 3. Left-panel: The Newton polytope associated with a one-loop massive triangle integral. Right-panel: Regions of the (x_1, x_2) -coordinate plane covered by each sector of the decomposition. The solutions of $\tilde{\mathcal{F}}(\mathbf{y}; \mathbf{s}) = 0$ are also shown for $\tilde{s} = 4$ and $\tilde{s} = 9$ after x_3 is eliminated using the delta-functional of Eq. (2.22).

Now, let us sector decompose this integral using the geometric approach [14, 49–53]. The first step of this algorithm is to re-express the integrand in terms of local variables obtained from the normal vectors of the facets of the Newton polytope of the integrand, depicted in Figure 3. The change of variables to the facet coordinates is given by,

$$x_1 \rightarrow y_1^{-1}y_3, \quad x_2 \rightarrow y_1^{-1}y_2. \quad (2.27)$$

Inserting this into $\tilde{\mathcal{F}}(\mathbf{x}; \mathbf{s})$ after integrating over x_3 using the delta-functional, we obtain,

$$\tilde{\mathcal{F}}(\mathbf{y}; \mathbf{s}) = y_1^{-2}(-\tilde{s}y_1y_3 + (y_1 + y_2 + y_3)^2). \quad (2.28)$$

The domain of integration is now the unit hypercube. The minimum value of \tilde{s} for which we can encounter a solution of $\tilde{\mathcal{F}}(\mathbf{y}; \mathbf{s}) = 0$ is again $\tilde{s} = 4$, which is obtained for $y_1 = 1, y_2 = 0, y_3 = 1$ (which corresponds to $x_1 = 1, x_2 = 0$).

In Figure 3, we depict the regions of the (x_1, x_2) -coordinate plane covered by each sector of the sector decomposition. The three sectors that form a sector decomposition of the integral are obtained by setting $y_1 = 1$ (red), $y_2 = 1$ (yellow) and $y_3 = 1$ (green), respectively. The coordinate $x_1 = x_2 = 1$ is the point at which the integral is divided by the geometric sector decomposition. In the first sector, obtained by setting $y_1 = 1$, the variety of $\tilde{\mathcal{F}}(\mathbf{y}; \mathbf{s})$ enters the sector at the point $y_2 = 0, y_3 = 1$ (which corresponds to $x_1 = 1, x_2 = 0$) with $\tilde{s} = 4$. In the third sector, obtained by setting $y_3 = 1$, the variety enters at the point $y_1 = 1, y_2 = 0$ (which again corresponds to $x_1 = 1, x_2 = 0$) with $\tilde{s} = 4$. However, for $\tilde{s} = 4$ the variety of $\tilde{\mathcal{F}}(\mathbf{y}; \mathbf{s})$ does not enter the second sector, obtained by setting $y_2 = 1$. Instead, we must have $\tilde{s} \geq 9$ before the threshold is encountered in this sector. In Figure 3, we depict the solutions $\tilde{\mathcal{F}}(\mathbf{x}; 4) = 0$ and $\tilde{\mathcal{F}}(\mathbf{x}; 9) = 0$. We can observe that the arbitrary choice of the sector decomposition point as $x_1 = x_2 = 1$ has determined the value of \tilde{s} for which the physical threshold first appears in the second sector.

In the triangle example considered, we can avoid distorting the threshold behaviour after sector decomposition by choosing a different hyper-surface in the delta-functional of Eq. (2.22) and/or by selecting a different sector decomposition point, which can be realised by rescaling the Feynman parameters by positive factors. However, public codes which automatically derive a sector decomposition of dimensionally regulated parameter integrals do not currently employ techniques to avoid distorting physical thresholds.

In the remainder of this work, we will assume that sector decomposition is applied as in the current public implementations. We must therefore devise a strategy for systematically finding the thresholds in each sector. This can be achieved using constrained numerical optimisation and/or gradient descent routines. For example, suppose we wish to find a positive \tilde{s} threshold in the k -th sector. First, we solve $F_k(\mathbf{y}; \mathbf{s}) = 0$ for \tilde{s} , let us label this solution $f_k(\mathbf{y}; \mathbf{s} \neq \tilde{s})$. Next, we may introduce a loss function,

$$L(\mathbf{y}; \mathbf{s}) = |f_k(\mathbf{y}; \mathbf{s} \neq \tilde{s})| + C \theta(-f_k(\mathbf{y}; \mathbf{s} \neq \tilde{s})), \quad (2.29)$$

where C is a large positive constant that imposes the correct sign of \tilde{s} and θ is the Heaviside function. We may then minimise this loss function subject to the constraint that $\mathbf{y} \in [0, 1]^N$, i.e. each variable remains in the unit hypercube. We will apply this procedure to an example integral in Section 6.

3 Optimal contour equivalence

In this section, we consider how the variance of the globally determined contour compares with one that would be optimised on a phase-space point-by-phase-space point basis. Let us consider the integrand,

$$f_\lambda(x_1, \dots, x_N; s_1, \dots, s_M), \quad (3.1)$$

where λ parametrises the contour deformation. The x parameters are the ones to integrate over, and the s parameters are the ‘physical’ parameters. For simplicity, we take the range

of $\mathbf{x} = (x_1, \dots, x_N)$ and $\mathbf{s} = (s_1, \dots, s_M)$ to be in the unit hypercube, with a mapping of the unit hypercube \mathbf{s} variables to the physical values between their minimum and maximum.

In a local integration strategy, for each set of parameters \mathbf{s} , the best path can be found by minimising the standard deviation of the integrand,

$$\sigma_{loc}^2(\mathbf{s}, \lambda) = \int d\mathbf{x} \left(f_\lambda(\mathbf{x}; \mathbf{s}) - \hat{f}(\mathbf{s}) \right)^2, \quad (3.2)$$

with respect to the path,

$$\lambda_{loc} = \arg \min_{\lambda} \sigma_{loc}^2(\mathbf{s}, \lambda), \quad (3.3)$$

with

$$\hat{f}(\mathbf{s}) = \int d\mathbf{x} f_\lambda(\mathbf{x}; \mathbf{s}). \quad (3.4)$$

To globally determine the contour, we minimise the standard deviation of the integrand over the full physical parameter range of \mathbf{s} instead of fixing its value and optimising at each phase-space point. The function to minimise is the standard deviation,

$$\sigma_{glob}^2(\mathbf{s}) = \int d\mathbf{s} \int d\mathbf{x} \left(f_{\lambda(\mathbf{s})}(\mathbf{x}; \mathbf{s}) - \bar{f} \right)^2, \quad (3.5)$$

where,

$$\bar{f} = \int d\mathbf{s} \int d\mathbf{x} f_\lambda(\mathbf{x}; \mathbf{s}), \quad (3.6)$$

is the average of the integral over the physical phase-space, \mathbf{s} . By definition of the contour deformation, \bar{f} is independent of the choice of contour, while σ_{glob}^2 can change.

It is instructive to decompose the standard deviation above,

$$\begin{aligned} \int d\mathbf{x} \int d\mathbf{s} (f_\lambda(\mathbf{x}; \mathbf{s}) - \bar{f})^2 &= \int d\mathbf{x} \int d\mathbf{s} \left(f_\lambda(\mathbf{x}; \mathbf{s}) - \hat{f}(\mathbf{s}) + \hat{f}(\mathbf{s}) - \bar{f} \right)^2 \\ &= \int d\mathbf{x} \int d\mathbf{s} \left(f_\lambda(\mathbf{x}; \mathbf{s}) - \hat{f}(\mathbf{s}) \right)^2 + \int d\mathbf{x} \int d\mathbf{s} \left(\hat{f}(\mathbf{s}) - \bar{f} \right)^2 \\ &\quad + 2 \int d\mathbf{x} \int d\mathbf{s} \left(f_\lambda(\mathbf{x}; \mathbf{s}) - \hat{f}(\mathbf{s}) \right) \left(\hat{f}(\mathbf{s}) - \bar{f} \right) \\ &= \int d\mathbf{s} \sigma_{loc}^2(\mathbf{s}) + \int d\mathbf{s} \left(\hat{f}(\mathbf{s}) - \bar{f} \right)^2, \end{aligned} \quad (3.7)$$

where we recognised in the first term the minimisation objective of the local contour optimisation and used the definition of $\hat{f}(\mathbf{s})$ to show that the mixed term vanishes. The minimum of the global objective is therefore not necessarily consistent with the minimum of individual local optimisations because of the influence of the second term.

If $\hat{f}(\mathbf{s})$ was known we could redefine,

$$f \rightarrow g(\mathbf{x}, \mathbf{s}) \equiv f(\mathbf{x}, \mathbf{s}) - \hat{f}(\mathbf{s}), \quad (3.8)$$

giving,

$$\hat{g}(\mathbf{s}) = \int d\mathbf{x} g(\mathbf{x}; \mathbf{s}) = \int d\mathbf{x} f(\mathbf{x}, \mathbf{s}) - \hat{f}(\mathbf{s}) = 0, \quad (3.9)$$

and

$$\bar{g} = \int d\mathbf{s} \int d\mathbf{x} g(\mathbf{x}; \mathbf{s}) = \int d\mathbf{s} \int d\mathbf{x} f(\mathbf{x}; \mathbf{s}) - \hat{f}(\mathbf{s}) = 0. \quad (3.10)$$

With this modification, the second term in Eq. (3.7) vanishes, while the first remains unchanged as,

$$\sigma_{loc}^2(\mathbf{s}) \rightarrow \int d\mathbf{x} (g_\lambda(\mathbf{x}; \mathbf{s}) - \hat{g}(\mathbf{s}))^2 = \int d\mathbf{x} (f_\lambda(\mathbf{x}; \mathbf{s}) - \hat{f}(\mathbf{s}) - 0)^2 = \sigma_{loc}^2(\mathbf{s}). \quad (3.11)$$

After modification, the optimal contours in the local and global approaches would be the same. Of course, the value $\hat{f}(\mathbf{s})$ is the value of the integration and is not known, but an approximation for it would lead to optimal contours for the global method being close to the optimal paths for the local method.

In practice, we augment our training with a network $m(\mathbf{s})$ that attempts to emulate $\hat{f}(\mathbf{s})$. We consider the loss,

$$L = \int d\mathbf{s} d\mathbf{x} (f_\lambda(\mathbf{x}; \mathbf{s}) - \bar{f} - (m(\mathbf{s}) - \bar{m}))^2 \quad (3.12)$$

where \bar{m} is the average of $m(\mathbf{s})$ and both the path λ and the approximation of the average $m(\mathbf{s})$ have neural network parameters to be optimised.

Note that there is a redundancy in the definition of $m(\mathbf{s})$: any constant shift is cancelled in the average subtraction. To prevent $m(\mathbf{s})$ from drifting to large values and induce numerical noise, it is useful to add a term in the loss that pins its average to the average of f , such that $m(\mathbf{s})$ will be optimised to be the integral of f for a fixed \mathbf{s} value. After this last modification, we obtain our loss function,

$$L_{\text{var}} = (\bar{f} - \bar{m})^2 + \int d\mathbf{x} d\mathbf{s} (f_\lambda(\mathbf{x}; \mathbf{s}) - \bar{f} - (m(\mathbf{s}) - \bar{m}))^2. \quad (3.13)$$

The relative weight between the two terms could be tuned, but given that the network can easily adjust the second term to vanish by an appropriate setting of the bias in its last layer, it is not an important consideration in practice.

4 Network design and training

In this section, we describe the design and training of the neural networks we use to define the contour deformations. The focus of this article is to demonstrate that such an approach can work and, in addition to providing a deformation *a priori*, yields improvements in the variance of the integrand. No extensive hyperparameter scan has been performed to optimise the learning rate, network size, activation function or the optimiser parameters.

4.1 Guided deformation

When the network is initialised, the deformation it represents might not represent a valid contour. To avoid this issue, we start the training with a large value of δ in Eq. (2.1), reducing it gradually to ensure the validity of the contours throughout the training.

This addresses the scale disparity issue on the input side. On the output side, the optimal values of λ can also span several orders of magnitude but must remain positive. To address this, we use the neural network, \mathcal{N}_λ , to predict the logarithm of λ ,

$$\lambda(s_1, \dots, s_M) = \exp(\mathcal{N}_\lambda(s_1, \dots, s_M)), \quad (4.1)$$

ensuring both positivity and a suitable scale coverage.

The approximation $m(\mathbf{s})$ of $\hat{f}(\mathbf{s})$ used to encourage the network to learn the locally best value of λ is also allowed to span several orders of magnitude by fitting the modulus and phase of the approximation,

$$m(s_1, \dots, s_M) = \exp(\mathcal{M}_r(s_1, \dots, s_M)) \exp(i\mathcal{M}_\phi(s_1, \dots, s_M)). \quad (4.2)$$

The functions \mathcal{N}_λ , \mathcal{M}_r and \mathcal{M}_ϕ are fully connected neural networks with \tanh activation functions. We use 4 layers of 40 units each.

The training is organised in two phases. The loss, given in Eq. (2.19) is the same in both phases. In the first phase, the value of δ is progressively reduced by a constant factor, but the learning rate is kept constant. Once the regulator δ has reached a small value, the second phase starts, where the learning rate is reduced by a factor when the validation loss reaches a plateau. We do not reduce the learning rate in the first phase because the loss is expected to increase as the regulator gets closer to 0, this is not a sign that the learning has stalled but an expected behaviour. When the integrand over the phase space considered for training spans several orders of magnitude, it is useful to normalise the variance by the approximation of the integral $m(\mathbf{s})$, so that the loss approaches the average of the relative variance. This modification is only effective once the approximation $m(\mathbf{s})$ has been learned for the true integrand, i.e. when the regulator has converged to 0. With this modification, the loss takes the form

$$L = \frac{L_{\text{var}}}{|m(\mathbf{s})|} + C \text{ReLU}(\text{Im}F(\mathbf{z}; \mathbf{s}))^2. \quad (4.3)$$

We run 3 independent trainings and keep the network which reached the lowest loss at the end of the training.

4.2 Free deformation

For the free deformations, we use a 3-layer network with 40 GELU⁵ [54] units for each integration dimension. We chose this activation function because we need it to be continuously differentiable for the computation of the Jacobian. These derivatives are computed through the chain rule, as outlined in Ref. [46]. For the simplest example, we use the same two phases as described for the guided deformation. For the more complex example of the 2-loop elliptic box integral, we start by training the network to match the guided deformation, and then allow it in the second phase to deviate from it to optimise the variance.

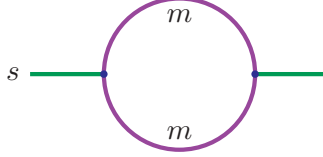


Figure 4. One-loop equal-mass bubble integral.

5 One-loop bubble example

The first example we consider is that of a scalar one-loop equal-mass bubble, see Figure 4. The integral is given by,

$$I(\mathbf{s}) = \Gamma(\epsilon) \int_{\mathbb{R}_{\geq 0}^2} dx_1 dx_2 \frac{(x_1 + x_2)^{-2+2\epsilon} \delta(1 - x_1 - x_2)}{(-sx_1 x_2 + m^2 (x_1 + x_2)^2 - i\delta)^\epsilon} = \Gamma(\epsilon) \int_0^1 dx \frac{1}{F(x, s)^\epsilon} \quad (5.1)$$

$$= \frac{1}{\epsilon} - \gamma_E - \int_0^1 dx \log(F(x, s)) + \mathcal{O}(\epsilon), \quad F(x, s) = -x(1-x)s + m^2 - i\delta, \quad (5.2)$$

where $s = p^2$ is the invariant mass squared of the incoming and outgoing momenta and m is the mass of the internal propagators. For $m > 0$ the integral is free of endpoint singularities and does not need a sector decomposition. We can factor out an overall m^2 and consider the integral as a function of $\tilde{s} = s/m^2$.

$$I(\mathbf{s}) = \frac{1}{\epsilon} - \gamma_E - \log(m^2) - \int_0^1 dx \log(\tilde{F}(x, \tilde{s})) + \mathcal{O}(\epsilon), \quad \tilde{F}(x, \tilde{s}) = -x(1-x)\tilde{s} + 1 - i\delta, \quad (5.3)$$

where the last term is the numerical integration we will consider. For $\tilde{s} > 4$, there are two singularities in the integration region, and a contour deformation is necessary.

For the 1-loop bubble integral the guided deformation of Eq. (2.7) is given by

$$z = x - ix(1-x)\tilde{s}(2x-1)\lambda. \quad (5.4)$$

We are ready to investigate the λ dependence of the integral variance. The left-hand pane of Figure 5 shows the dependence of the variance of the integrand as a function of the deformation λ for set values of \tilde{s} . In general, we would expect a small value of the deformation to lead to a large variance, because the integration path is close to the poles on the real axis. In this example, the variance reaches a plateau for small values of the deformation. This is because the exponent of the F polynomial in the denominator of Eq. (5.1) is ϵ and therefore there is no singularity in the integrand.

Too large a deformation also leads to an increased variance, this time due to the large added imaginary part. Given the simplicity of the integral, we can compute the value of the

⁵The activation function for the GELU (Gaussian Error Linear Units) is $\text{GELU}(x) = x \Phi(x)$, where $\Phi(x)$ is the Cumulative Distribution Function for the Gaussian Distribution.

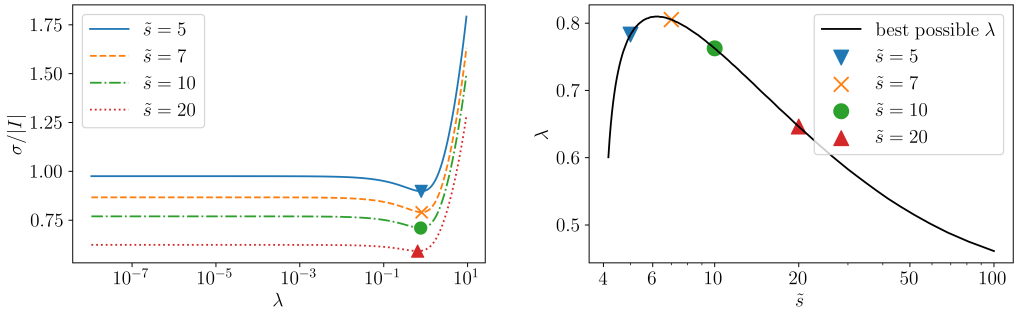


Figure 5. Left-hand: variance of the integrand normalised by the integrand as a function of λ for a selection of values of \tilde{s} . The markers show the position of the minimum. Right-hand pane: value of lambda that minimises the variance of the integrand. The markers correspond to the values of the minima for the curves on the left-hand side plot.

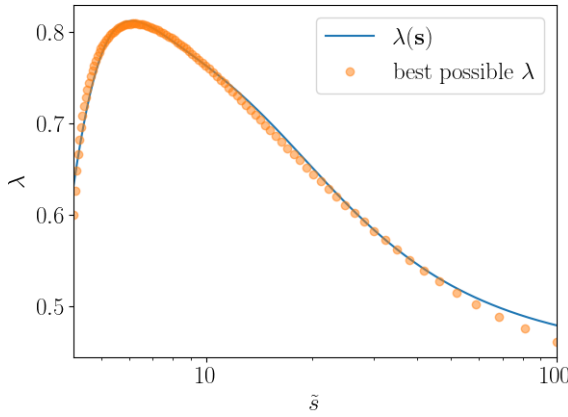


Figure 6. Comparison of the optimal values of λ compared with the values determined by the guided deformation neural network.

variance of the integrand as a function of λ and numerically determine the optimal value of λ for each value of \tilde{s} . The right pane of Figure 5 shows the value of λ that minimises the variance of the integrand as a function of \tilde{s} . For large values of \tilde{s} , the poles are situated close to the boundaries of integration, and it becomes beneficial to have a larger slope, see Figure 11.

We now want to test a neural network determination of the λ value to use. We consider the range $4.01 < \tilde{s} < 100$. After training, the values of λ obtained match the optimal ones very well, as can be seen from Figure 6.

We could also apply the modification described in Section 3 (i.e. we can subtract the estimated value of the integrand, $m(\mathbf{s})$), but this has almost no effect since the values of λ obtained without the modification are already very close to their optimal value. This is because the contribution to the variance coming from the variance of $\hat{f}(\mathbf{s})$ (the first term in the right-hand side of Eq (3.7)) is negligible compared to that coming from the integrand

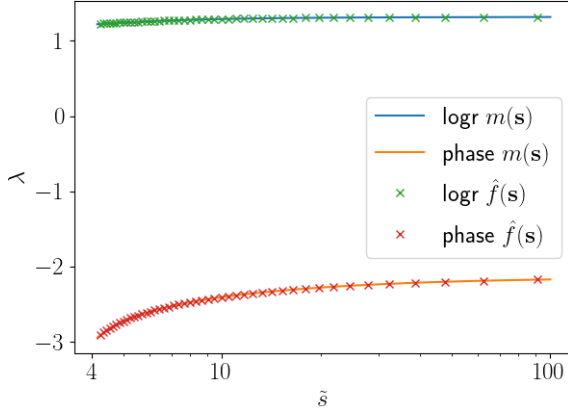


Figure 7. Comparison of the true value of $\hat{f}(\mathbf{s})$ and its approximation $m(\mathbf{s})$. The values are expressed in polar coordinates, and we plot the logarithm of the radius along with the argument of the true value of the integral for fixed \tilde{s} (crosses) and its approximation $m(\mathbf{s})$ (solid line).

variance at fixed values of \tilde{s} (the second term in the right-hand side of Eq (3.7)).

5.1 Free deformation

We now turn to the deformation where the λ_i are allowed to take the much more flexible form of a function of both the kinematic invariants and the integration variables; $\lambda_i := \lambda_i(x_1, \dots, x_N; s_1, \dots, s_M)$. We train this deformation with the modification described in Section 3. First, we can verify that the neural network was able to get a good approximation $m(\mathbf{s})$ of $\hat{f}(\mathbf{s})$. This is shown in Figure 7 where we compare the neural network approximation to the true value of $\hat{f}(\mathbf{s})$ obtained through direct numerical integration.

On the left-hand side of Figure 8, we compare the variance of the integrands obtained with the guided deformation and those obtained using a neural network. We can see that the free deformation achieves a lower variance. This is not very surprising given that they have a much less restricted functional form, and, given enough parameters, the full neural network solution should at least be able to match the guided deformation results by matching its functional form. On the same plot we show the variance from the deformation selected by pySECDEC, which in this case is $\lambda = 1$ because of the limit on the maximum size of the deformation described in Section 2.4.

An improvement in the variance of the integrand translates directly to a better performance for a standard Monte Carlo integration. In practice, for large dimensions, a QMC is often used instead of conventional MC, and there is no guarantee that an improvement in the variance translates into an improvement in the QMC performance. If we plot the estimated error from 32 random shifts of a lattice computed with the median of means method with 21 candidates, we find the first example of a somewhat counter-intuitive result of this article: the improvement of the variance does not always translate into an improvement of the QMC performance. This is illustrated in the right-hand side of Figure 8 for a lattice size

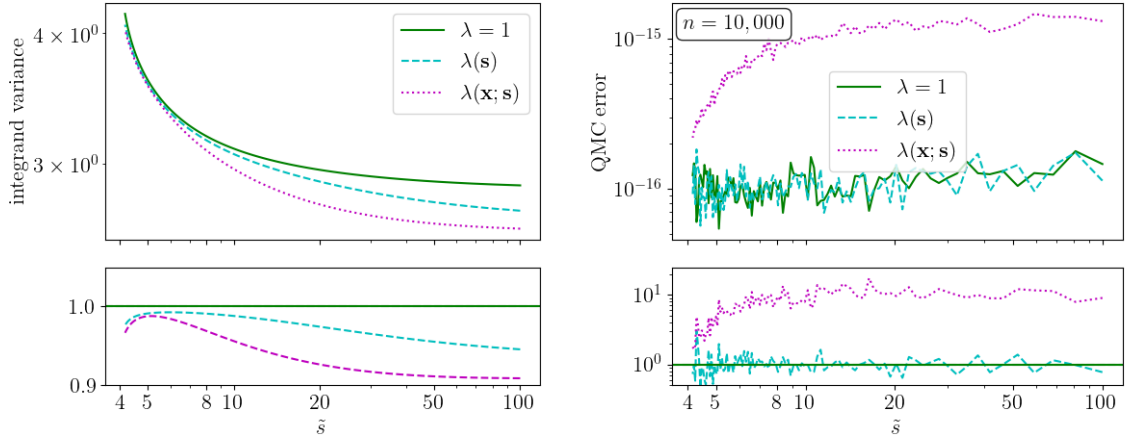


Figure 8. Comparison of the variance of the guided deformation and the neural network deformation. Left pane: variance of the integrand. Right pane: ratio of the variance obtained from the two methods.

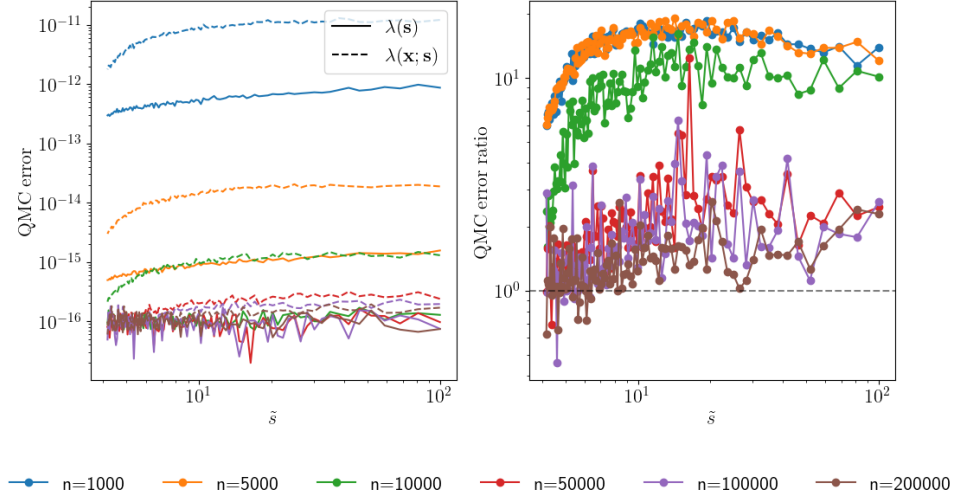


Figure 9. QMC performance comparison between the guided deformation and the neural network deformation as a function of the lattice size. Left pane: QMC error estimate as a function of the lattice size. Dashed lines correspond to the $\lambda(\mathbf{x}; \mathbf{s})$ neural network deformation and solid lines to the $\lambda(\mathbf{s})$ deformation. Right pane: The curves show the ratio of the QMC error estimates from the neural network deformation to those from the guided deformation.

of 10,000⁶. The QMC error estimate does not change significantly when the deformation is only rescaled from $\lambda = 1$ to $\lambda(\mathbf{s})$, but it changes when the functional form is altered using $\lambda(\mathbf{x}; \mathbf{s})$. Plotting the free and guided QMC error estimate for a variety of lattice sizes in Figure 9 shows that the effect is not limited to a single lattice size and seems systematic, but decreases with large lattice sizes.

In Figure 10 we plot the dependence of the QMC error estimate as a function of the

⁶whenever we refer to a lattice size N , we mean "the first prime integer larger than N ."

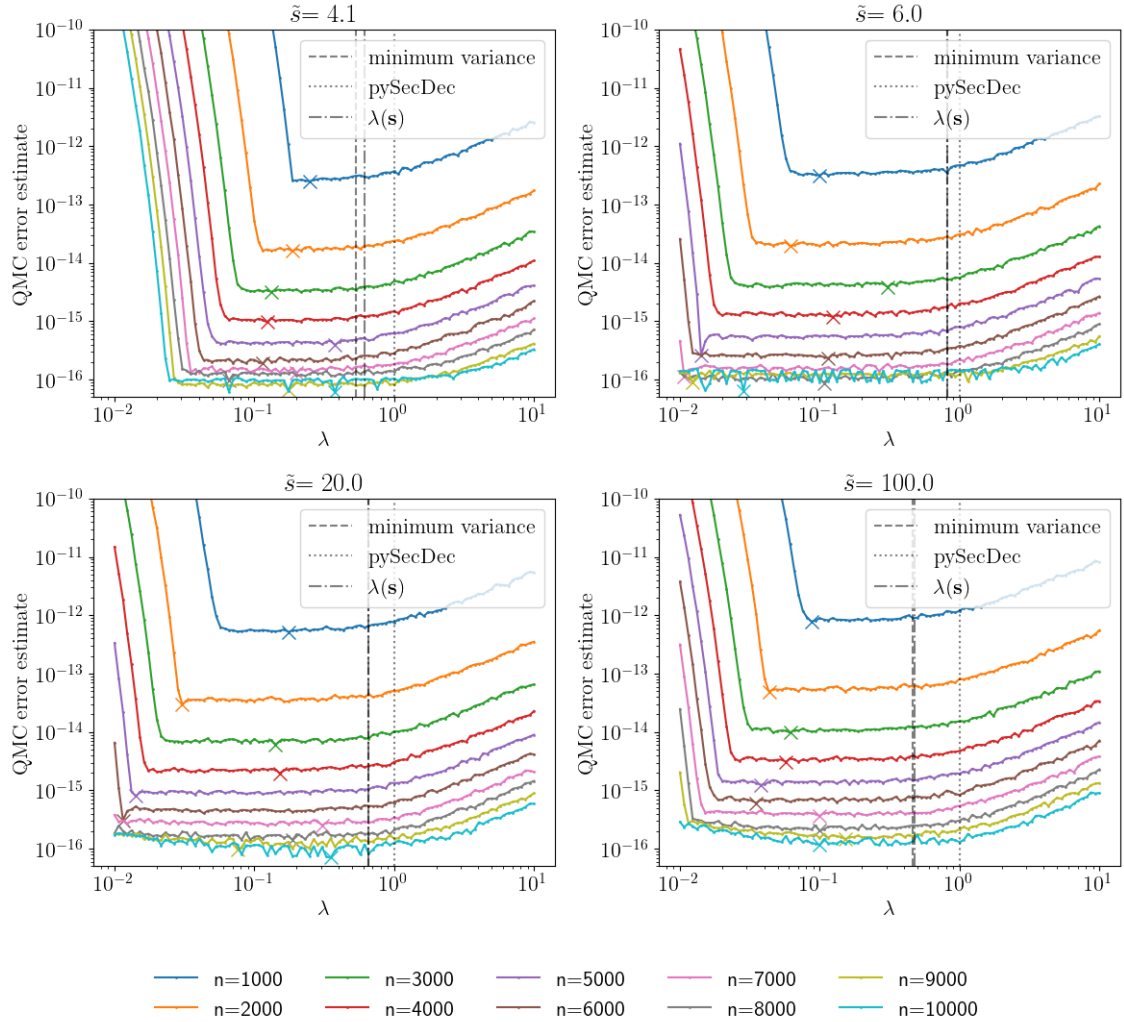


Figure 10. QMC performance as a function of the deformation strength λ for a set of lattice sizes. The dashed vertical line corresponds to the optimal value of λ to minimise the integrand variance. The crosses show the minimum of the QMC error estimate, whose location has a strong dependence on the grid size.

lattice size. We see that the optimal contour for the purpose of minimising the QMC error depends on the lattice size. While the optimal contour from the integrand variance point of view is independent of the lattice size, this dependence means that there is no unique optimal contour for QMC integration. We note that for this integral there is a plateau of good λ choices and both the optimal λ choice for a given lattice and the λ that minimises the variance are close to this plateau.

It would be interesting to investigate the behaviour of the minimum of the QMC error estimate for large lattice sizes, but as can be seen in the left-hand pane of Figure 9, lattice sizes above 50000 reach the limit of the numerical accuracy one can expect from double-precision floating point operations.

For this one-dimensional integral, it can be instructive to visualise the deformations.

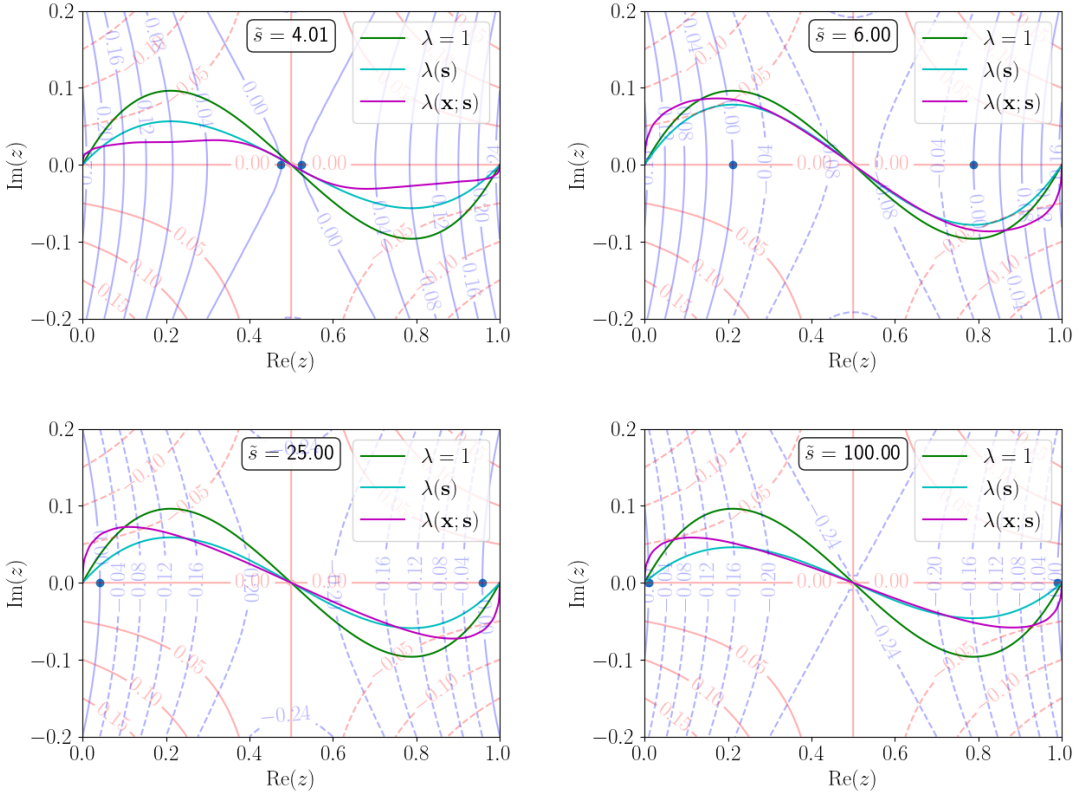


Figure 11. Deformed path for the guided and neural network deformations for three values of \tilde{s} : 4.01 (top left), 6 (top right), 25 (bottom left), 100 (bottom right). The faint blue and red lines show contours of constant real and imaginary part of the F polynomial, respectively.

Figure 11 shows the deformed path for three different values of \tilde{s} . The shape of the free deformation visibly differs from the guided and heuristic deformations. For the phase-space points considered, it always has a steeper start at the integration boundaries and a smaller magnitude than picked using the heuristic approach.

6 Two-loop box integral example

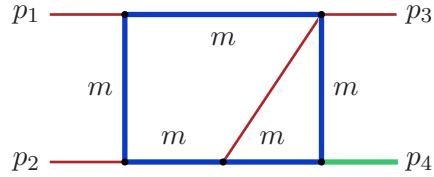


Figure 12. Feynman diagram for the two-loop elliptic box integral. Figure adapted from Ref. [33].

We consider a two-loop integral defined by the Feynman diagram of Figure 12. The

integral can be written as⁷,

$$I(\mathbf{s}) = \Gamma(2\epsilon + 2) \int_{\mathbb{R}_{\geq 0}^6} \prod_{i=1}^6 dx_i \frac{\mathcal{U}(\mathbf{x})^{3\epsilon}}{(\mathcal{F}(\mathbf{x}; \mathbf{s}) - i\delta)^{2\epsilon+2}} \delta(1 - x_6), \quad (6.1)$$

where the \mathcal{U} and \mathcal{F} polynomials are given by,

$$\begin{aligned} \mathcal{U}(\mathbf{x}) &= x_3 x_4 + x_3 x_5 + x_4 x_5 + (x_4 + x_5) x_6 + x_1 (x_3 + x_5 + x_6) + x_2 (x_3 + x_5 + x_6), \\ \mathcal{F}(\mathbf{x}; \mathbf{s}) &= -((tx_4 x_5 + p_4^2(x_3(x_1 + x_2 + x_4) + (x_2 + x_3)x_5))x_6) - s x_1 (x_3 x_5 + x_2 (x_3 + x_5 + x_6)) \\ &\quad + m^2(x_1 + x_2 + x_3 + x_4 + x_6)(x_3 x_4 + x_3 x_5 + x_4 x_5 + (x_4 + x_5)x_6 + x_1 (x_3 + x_5 + x_6) \\ &\quad + x_2 (x_3 + x_5 + x_6)). \end{aligned}$$

The external legs p_1 , p_2 and p_3 are massless, and p_4 is massive. We consider the physical region with p_1, p_2 incoming and p_3, p_4 outgoing. This integral has physical thresholds at $s = (p_1 + p_2)^2 = 4m^2$, $p_4^2 = 4m^2$ and $t = (p_1 - p_3)^2 = 4m^2$. For the remainder of this section, we consider the integral for $m^2 = 1$ (or, equivalently, as a function of the rescaled parameters s/m^2 , t/m^2 and p_4^2/m^2). The integral has endpoint divergences and requires a sector decomposition. Applying geometric decomposition as implemented in pySECDEC yields 22 sectors⁸. The labelling of the sectors has no intrinsic meaning⁹, but they are consistent throughout this work. To each sector integral, a Korobov transformation with $\alpha = \beta = 3$ is applied to improve the error convergence of the QMC integrator [12].

As described in Section 2.5, after sector decomposition, the physical thresholds can move, and they can pick up additional dependencies on physical parameters. The location of the lowest threshold in s , that is, the smallest value of s at which a given sector develops an imaginary part, is displayed in Figure 13. The location of the threshold for each sector can be determined numerically by investigating the corresponding F -polynomial. First, we insert the value of p_4^2 and $m^2 = 1$, then substitute

$$t \rightarrow -\tau(s - p_4^2)$$

where $\tau \in [0, 1]$ covers all allowed values of t . At this point, in each sector, the $F(\mathbf{y}; \mathbf{s})$ polynomial is a linear function of s with coefficients that are functions of the facet variables, \mathbf{y} , and τ . We solve the equation $F(\mathbf{y}; \mathbf{s}) = 0$ for s and obtain

$$s = f(\mathbf{y}; \mathbf{s} \neq \tilde{s}), \quad (6.2)$$

which we numerically minimise over the unit hypercube spanned by \mathbf{y}, τ . This procedure will find the smallest value of s for which $F(\mathbf{y}; \mathbf{s}) = 0$ has a solution, and therefore the location of the threshold. The numerically found solutions can be verified analytically.

In the first part of this section, we will work with a fixed value of $p_4^2/m^2 = 12/23$, which approximates the ratio m_t^2/m_H^2 , where m_t is the on-shell top-quark mass and m_H is the on-shell Higgs boson mass. In the second part of this section, we will relax this constraint to

⁷The Cheng-Wu theorem has been used to change $\delta(1 - \sum_i x_i) \rightarrow \delta(1 - x_6)$.

⁸With `decomposition_method=geometric`, see Ref. [53] for a description of the implementation.

⁹Indeed, pySECDEC might return them in a different order for each call.

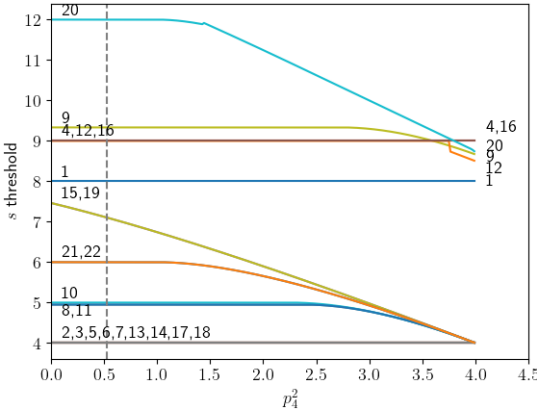


Figure 13. Lowest s threshold as a function of p_4^2 . Several curves overlap for some sectors; their number(s) is displayed close to the respective curve. The vertical line corresponds to the value $p_4^2/m^2=12/23$ used for the numerical evaluation of these sectors in this work.

| $s_{threshold}^{(k)}$ | numerical | sector (k) |
|--------------------------|---------------|-----------------------|
| 4 | 4 | 2,3,5,6,7,13,14,17,18 |
| $5/2 + \sqrt{6}$ | $\simeq 4.95$ | 8,11 |
| 5 | 5 | 10 |
| 6 | 6 | 21,22 |
| $2/23(37 + \sqrt{2001})$ | $\simeq 7.1$ | 15,19 |
| 8 | 8 | 1 |
| 9 | 9 | 4,12,16 |
| $28/3$ | $\simeq 9.3$ | 9 |
| 12 | 12 | 20 |

Table 1. Lowest s thresholds for each sector, $s_{threshold}^{(k)}$. The non-integer values are algebraic functions involving the value $12/23$ used as the ratio p_4^2/m^2 .

facilitate comparison with previous work. We will investigate the deformations to evaluate it in three regions: $1 < s < s_{threshold}^{(k)}$, $s_{threshold}^{(k)} < s < 100$ and $100 < s < 10,000$ where the separation point, $s_{threshold}^{(k)}$, is sector dependent, and given in Table 1.

For fixed p_4^2/m^2 , the F polynomial for each sector scales with at most one power of s/m^2 or t/m^2 . This also means that the derivative of F entering Eq. (2.7) scales with s/m^2 and t/m^2 . In the physical region where s or t are large, this leads to large deformations, to counterbalance this effect, we scale the value of λ predicted by the network by $1/s$. In principle, the network could learn this functional dependence, but the training would be more difficult, and the issue of large initial deformation not being valid (see Section 4) would be exacerbated.

Since we are considering a wide range of scales, especially in the large- s region, we first

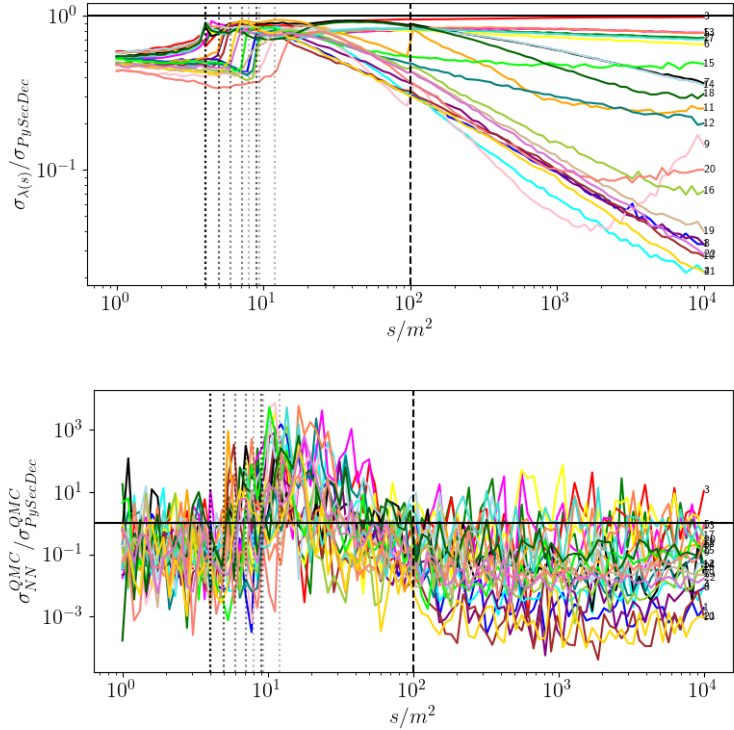


Figure 14. Upper plot: Ratio of the standard deviation of the integrand for the $\lambda(s)$ deformation to the pySECDEC integrand. Lower plot: ratio of the standard deviation of the shift ensemble for a lattice size of $2 \cdot 10^6$. The vertical lines show the location of the thresholds and the separation of the large \tilde{s} region, where discontinuities can be expected.

apply the transformation

$$s \rightarrow \log(s), \quad t \rightarrow -\frac{t}{s} \in [0, 1] \quad (6.3)$$

before standardisation and evaluation of the neural network.

6.1 Results

To assess the suitability of the deformation from our methods, we compare two quantities. The first is the variance of the integrand. For this, we expect the NN-guided method to yield a better result, since this is what the training is aimed at. Since we minimise this variance for a range of values of the physical parameters, some regions may underperform the pySECDEC variance, because their contribution to the loss is too small to be prioritised in the learning process. In other words, the noise in the regions where the integrand is large prevents the network from learning the optimal choice for the regions where the integrand is much smaller. We consider a one-dimensional slice where the value of t is fixed at the middle value of the allowed interval,

$$t = \frac{1}{2} (t_{\min} + t_{\max}), \quad t_{\min} = -s + p_4^2, \quad t_{\max} = 0. \quad (6.4)$$

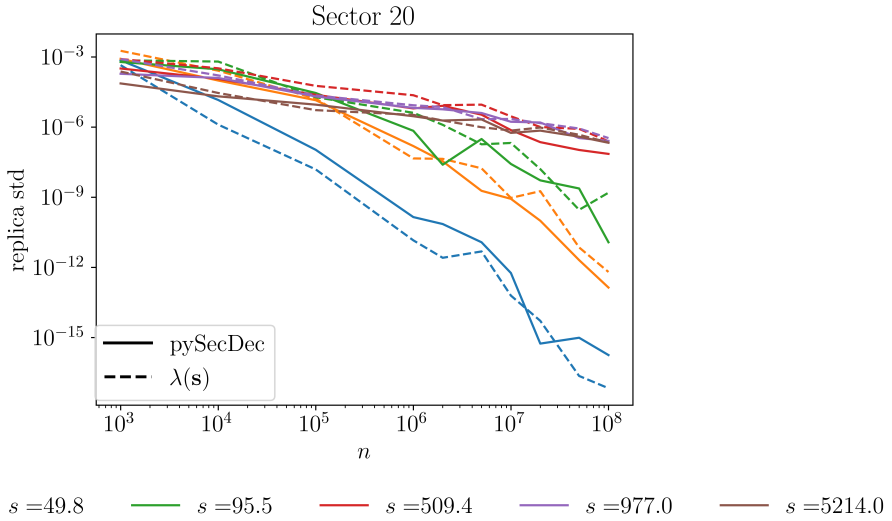


Figure 15. QMC error estimate of sector 20 as a function of the lattice size for different values of s .

We run pySECDEC for this range of s and t and record the final value of the deformation parameters λ . We then compare the variance of the integrand and the QMC error estimate with those obtained through our neural network.

The upper pane of Figure 14 shows the ratio of the variance of the integrand obtained from the NN-guided method to pySECDEC. Each sector is shown as a line. We can see that for most regions and most sectors, the variance is indeed reduced. The variance is evaluated using a QMC integration.

The second quantity we consider to assess the suitability of the NN-chosen contours is the error estimate from the QMC integration. To obtain this estimate, we follow the method described in Ref. [55]. For a given prime n , we generate n_l random lattices and select the random lattice with the median mean. For this lattice, we generate n_s random shifts and use the mean of the results from these n_s shifted lattices as the integral estimate and the standard deviation of the n_s results as the error estimate. We repeat a QMC integration with a given lattice n_s times, each with a different random shift. The standard deviation of the results gives an estimate of the error of the QMC integration. In principle, a better-behaved integrand yields a lower error estimate. We find that reducing the variance of the integrand is not a guarantee that the QMC error estimate will be reduced. The lower pane of Figure 14 shows the ratio of the QMC error estimates between the contour chosen by the neural network and the one chosen following the pySECDEC procedure for a lattice size of 2 million points. We see that in some cases this ratio can take dramatically large values, although the integrand has a small variance.

In Figure 15, we see that the scaling of the QMC error estimate with the number of lattice points is similar for both methods of choosing a contour, although the error obtained with the two methods can differ significantly.

In Figure 16, we investigate the dependence of the QMC error as a function of both

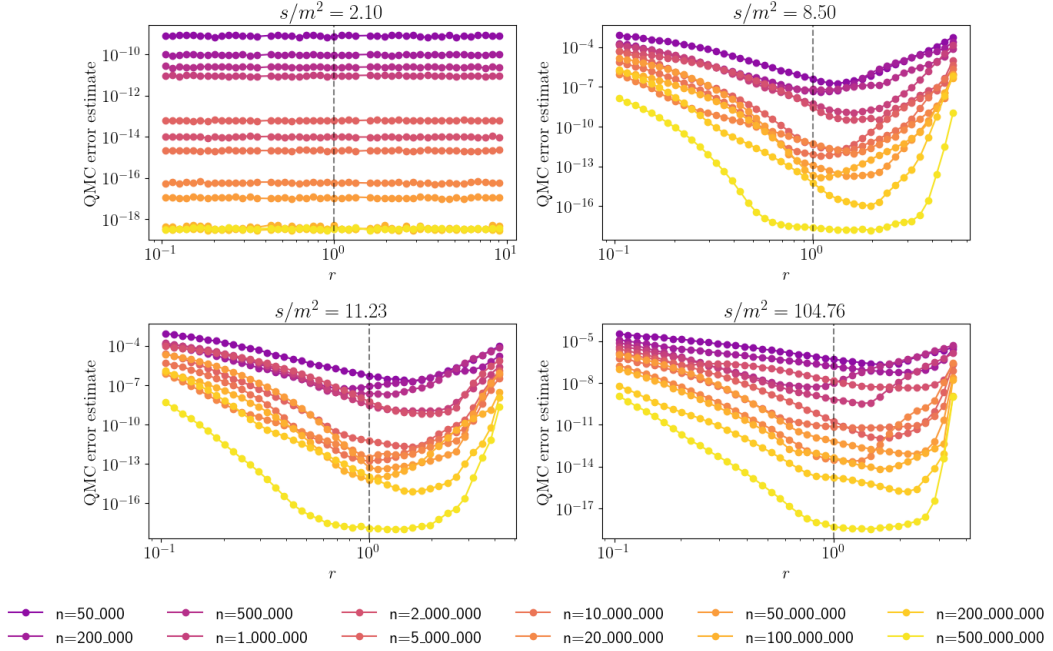


Figure 16. QMC error estimate for sector 11 as a function of the rescaling of the deformation strengths λ_i by a fixed scalar r for different lattice sizes. The dashed line shows the λ value that minimises the variance of the integrand.

the deformation parameter and the lattice size. To do so, we take a reference value of λ_i and rescale all components by a fixed factor r . The reference value of λ_i is obtained by numerically minimising the variance as a function of the deformation parameters λ_i . We take as a starting point the value given by the guided deformation found by the neural network training. Too large values of r may describe an invalid shift, so we check that for the data points plotted, the value of the integrand has not departed too much from its true value. We can see that the minimum of the QMC error estimate does not match the value that minimises the variance, but it appears to be the case that as the lattice size increases, the optimal QMC λ converges to the value that minimises the variance. Given that there is no unique choice of λ that would be optimal for all lattice sizes, choosing the values that minimise the variance does not appear to be a bad choice.

The curves showing the behaviour of the QMC error estimate on the rays defined above are shown in Figure 16. Again, we see that the optimal contour for the purpose of QMC error estimate optimisation is dependent on the lattice size. We also note that there are many crossovers between curves corresponding to different lattice sizes. When this happens, and a curve for a lower lattice size crosses that of a larger size, this means that the QMC error estimate will grow despite an increase in lattice size. These counterintuitive situations illustrate one of the complexities of QMC integration.

Figure 17 shows a comparison of the lambda values from pySECDEC and from our guided deformation for the first four sectors. The comparison for all sectors is shown in Appendix B. We observe that the λ values selected by the neural network have a much

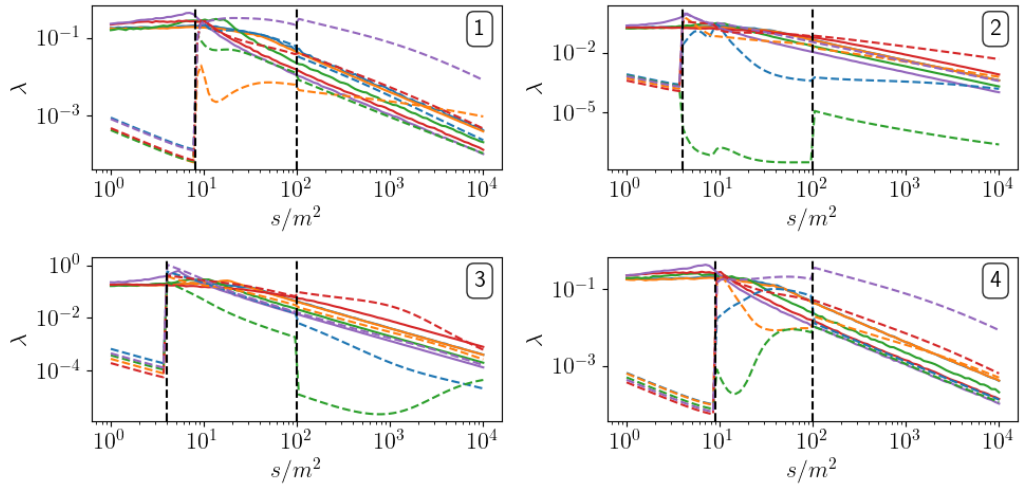


Figure 17. Comparison between the λ values for pySECDEC (solid) and the NN-guided values (dashed). Curves of the same colour correspond to the deformation strength for the same coordinate. The sector number is displayed in the upper right of each plot. The vertical dashed lines show the separation between different trainings, where discontinuities can be expected.

larger range of values and that the scale of the deformations applied to each parameter differs more for the neural network approach than the heuristic approach.

6.2 Free deformation

Allowing the deformation to now depend also on the sampling point x_1, \dots, x_N , such that $\lambda_i := \lambda_i(x_1, \dots, x_N; s_1, \dots, s_M)$, we can improve on the results of the previous section. Figure 18 shows the ratio of the variance obtained with free deformation over that obtained from the guided deformation. For $s < 4$ the improvement is hardly perceptible, due to the fact that the guided deformations are already almost optimal (almost vanishing). Between the thresholds, the improvements are visible but not substantial. Above threshold, the picture is slightly mixed. There are some large improvements, especially at very large values of s , but at the cost of a small loss of performance at moderate s values. This is likely due to limitations of the training and compromises made between different s and t regions. More parameters and/or more training would reduce the variance further.

6.3 Comparison with alternative neural network approach

In this section, we compare our approach with that of Ref. [33], where the authors investigated two *local* ways of determining the deformation. The first is similar to the NN guided deformation, in that the parameters λ of the deformation are determined by minimising the variance of the integrand, but unlike in our approach, that minimisation is repeated for each phase-space point. The second combines it with normalising flows to further improve the variance of the integrand. The training of the normalising flow is also performed for each phase-space point independently. We specifically compare their results for the “elliptic2L” integral and focus on their Figure 8. This integral corresponds to our sector 19 in

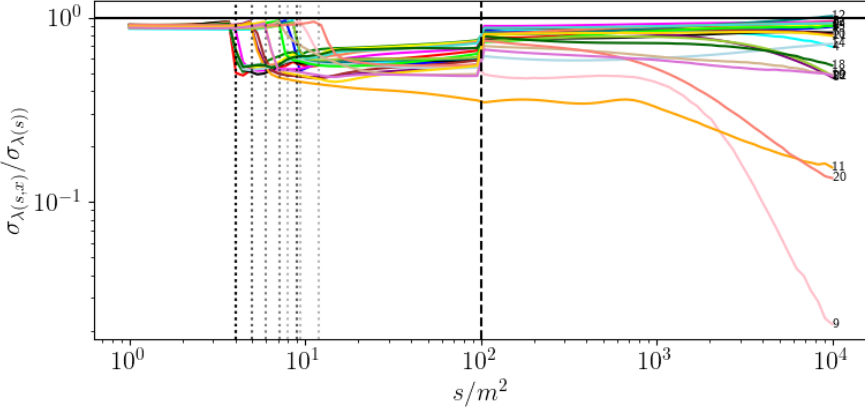


Figure 18. Ratio of the free deformation variance over the NN-guided variance for all 22 sectors of the 2-loop elliptic integral.

the previous section, but with p_4^2 not set to the fixed value 12/23. With the help of the authors, we reproduce this plot in the top row of Figure 20. Note that Ref. [33] did not use a Korobov transformation in their analysis. To facilitate comparison, we also refrain from using one in this section.

This plot was obtained setting $m^2 = 1$ and sampling points in two regions, one with moderate $s < 100$ and one with large values of $100 < s < 7000$. These points are displayed the left-hand side of Figure 19. In the larger s sample, we observe a larger spread of variances. This is due to the way the phase-space points were chosen. On the right-hand side of Figure 19, we plot the value of the external mass p_4^2 and s . For $s < 100$, the external mass was chosen according to $p_4^2 < 2$, instead, for larger values of s , the external mass was varied in the range $p_4^2 < 100$. At the value $p_4^2 = 4$, a new threshold appears, which explains the different behaviour. If we restrict the plot to those points with values of p_4^2 below this threshold, we obtain a more continuous plot, as shown in the middle row of plots in Figure 20. This threshold is not an issue for the method of Ref. [33], as each phase-space point is treated independently, but for our method it is important to separate them, as the optimal contour parameters cannot be expected to be continuous over the threshold, and the presence of a divergence in the middle of a training sample can cause significant issues with convergence and lead to non-optimal results.

Figure 19 (right-panel) shows the value of the imaginary part of the integrand. Phase-space points with a small value of the imaginary part (up to our numerical integration precision) correspond to the Euclidean region, and points with a non-vanishing imaginary part demonstrate the appearance of a threshold. The figure shows the two thresholds, the sector decomposition procedure shifts the $s = 4$ threshold, while the $p_4^2 = 4$ threshold remains unshifted. The phase-space points selected in Ref. [33] are shown in red. The point denoted by a cross, located close to the s threshold, is the outlier in the plot in the top row of Figure 20. This figure explains the existence and location of the outlier. In Appendix A we derive an analytical form for the threshold as a function of p_4^2 .

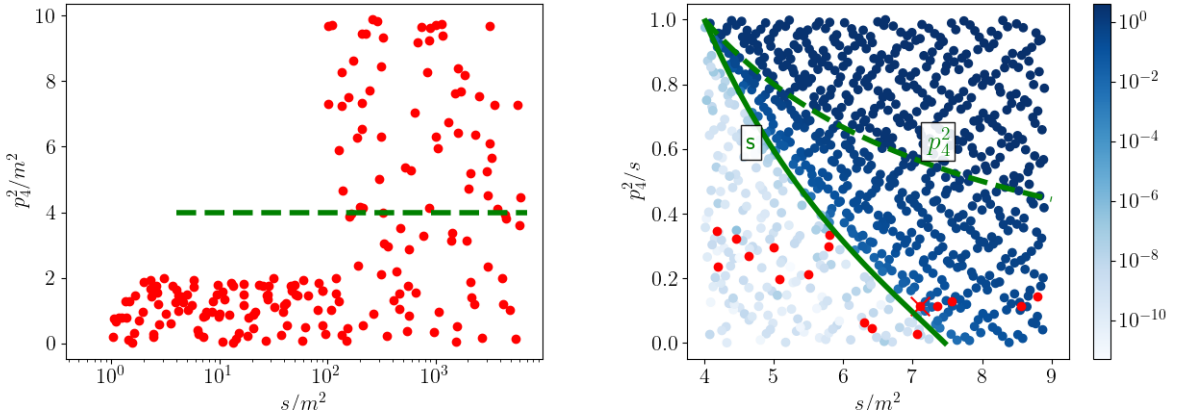


Figure 19. Left-hand panel: Distribution of sampled points in Figure 8 from [33]. The green line shows the location of the $p_4^2 = 4m^2$ threshold. Right-hand panel: threshold location for Sector 1 of Ref. [33]. The two green curves are the thresholds in the s and p_4^2 channels. The colour scale shows the magnitude of the imaginary part of the integrand. The red dots represent points sampled in Ref. [33] and the cross marks the location of the points giving rise to outliers in Figure 20.

Now that we have gained a better understanding of the features of the plot we wish to compare to, we add the result of our methods in the bottom row of Figure 20. We observe that our methods yield improved performance, although they are trained once over entire phase-space regions and not repeatedly for each phase-space point. In the Euclidean region (to the left of the green line on the right side of Figure 19), we observe that the $\lambda(\mathbf{s})$ and $\lambda(\mathbf{x}; \mathbf{s})$ methods perform similarly to each other and better than the pySecDec heuristic choice and Λ -glob, but worse than Λ -glob + Flow, in this region a good contour can be obtained with no deformation. Immediately above the s threshold, $\lambda(\mathbf{s})$ performs similarly to Λ -glob and $\lambda(\mathbf{x}; \mathbf{s})$ provides better performance, but still slightly worse than Λ -glob + Flow. At very large values of s , $\lambda(\mathbf{s})$ performs similarly to Λ -glob + Flow, with $\lambda(\mathbf{x}; \mathbf{s})$ providing the best performance.

7 Discussion

One could imagine using a different loss to optimise the QMC integration error estimate rather than the variance of the integrand, but there are some issues with this endeavour:

- The discussion of Section 3, where the equivalence of local and global optima is demonstrated, would need to be established for a loss function based on the QMC error estimate.
- The QMC loss has a strong dependence on the size of the lattice, as seen in Figure 10 and Figure 16, and it is impossible to make a choice of lambda that is simultaneously optimal for all lattice sizes. Furthermore, the QMC error is not a monotonic function of the lattice size. The error estimation of QMC integration is still not completely understood and is the subject of current research, see Ref. [56] for a recent status.

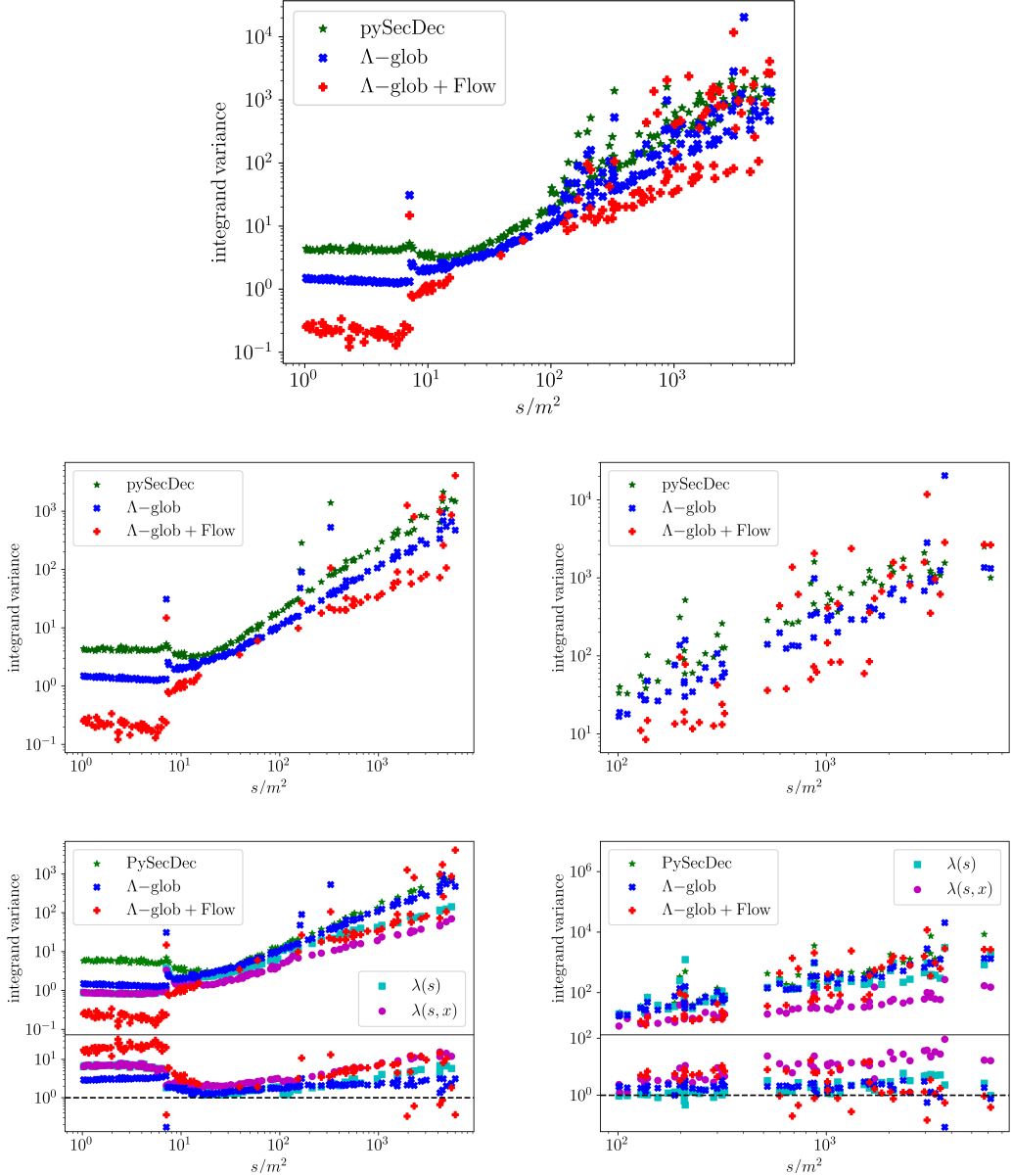


Figure 20. Top row: Reproduced Figure 8 from [33]. The y -axis has been rescaled to display the integrand variance rather than the relative error (shown in the original plot). Middle row: data from the top row separated according to the location with respect to the p_4^2 threshold. The right pane shows only points for which $p_4^2 < 4m^2$. The left pane shows those for which $p_4^2 > 4m^2$, this region was only sampled for values of $s > 100$, see Figure 19. In the lower row the results using the $\lambda(\mathbf{s})$ and $\lambda(\mathbf{x}; \mathbf{s})$ networks, produced in this work, are also shown. Following the choice made in [33], the ratio plot shows the variance improvement over the pySECDEC contour, therefore higher is better.

Using the methods demonstrated in this article as a replacement for the default deformation has the following potential efficiency savings in pySECDEC (and other similar programs):

- If a valid deformation is given without the need for pre-sampling, the first stage of the integration can be skipped.
- The computation time associated with iterations of the integration with non-valid deformations is avoided.

The use of the technique is only beneficial if the gains above are amortising the computing time needed to train the networks.

We considered two types of deformations. The guided NN is a lot easier to integrate into existing tools as only the new values of λ_i have to be passed. Indeed it is already implemented in pySECDEC. The free deformation requires providing both the deformed contour and the Jacobian for each lattice point evaluated, and the mechanism to do so would need to be efficiently implemented.

8 Conclusion

In this article, we have investigated the task of determining a valid contour deformation for a range of physical parameters *ab initio*, that is, before numerical integration for a fixed set of physical parameters is started. The ability to determine contours in this manner removes the need to find valid contours on a phase-space-by-phase-space basis, potentially improving the performance of existing tools for the evaluation of Feynman integrals in the physical Minkowski regime. Furthermore, knowledge of a function that can return valid contours of integration globally allows integration techniques that require the rapid evaluation of the integrand as a function of the phase-space, such as the neural network technique of Ref. [46], to be employed.

We have demonstrated that this task can be accomplished using Neural Networks and present two techniques, one which returns the magnitude of the deformation as a function of the phase-space point only, and another that returns for each phase-space point a deformation function depending on the integration variables. We show that by first finding the thresholds appearing in each sector of the integrand and then training a Neural Network for each kinematic region bounded by these thresholds, it is possible to construct a function that returns optimal contours of integration globally (i.e. contours which yield an integrand with minimal variance and which perform as well as contours optimised for a specific local phase-space point). We observe that although such contours are not optimal for QMC methods of integration, in fact, no contour is optimal for all lattice sizes, the performance of the contours is, nevertheless, very competitive with other heuristic and local methods of determining integration contours.

We compare the performance of our techniques to the previous work on determining optimal contours, presented in Ref. [33], and observe that our procedures compare favourably. However, in the present work, we need to train a Neural Network only once per region of

phase space, rather than individually for each phase-space point. This means that when evaluating a large number of phase-space points, the potentially substantial time required to train a Neural Network can be offset by the time-saving of not having to optimise the contour for each phase-space point. We leave a further detailed study of the performance of our contour deformations to future work.

Acknowledgments

It is our pleasure to thank Vitaly Magerya for the discussion of the interplay of sector decomposition and physical thresholds, and Vitaly Magerya and Ramon Winterhalder for clarifications and the sharing of the raw data and code of Ref. [33]. We also thank the other members of the pySECDEC collaboration for useful discussions; Gudrun Heinrich, Bakar Chargeishvili, Matthias Kerner, Vitaly Magerya and Johannes Schlenk. This research was supported in part by the UK Science and Technology Facilities Council under contracts ST/X000745/1 and ST/X003167/1. SJ is additionally supported by a Royal Society University Research Fellowship (URF/R1/201268, URF/R/251034).

References

- [1] R.J. Eden, P.V. Landshoff, D.I. Olive and J.C. Polkinghorne, *The analytic S-matrix*, Cambridge Univ. Press, Cambridge (1966).
- [2] H.S. Hannesdottir and S. Mizera, *What is the $i\varepsilon$ for the S-matrix?*, SpringerBriefs in Physics, Springer (1, 2023), [10.1007/978-3-031-18258-7](https://doi.org/10.1007/978-3-031-18258-7), [2204.02988].
- [3] E. de Doncker, Y. Shimizu, J. Fujimoto, F. Yuasa, K. Kaugars, L. Cucos et al., *Loop integration results using numerical extrapolation for a non-scalar integral*, *Nucl. Instrum. Meth. A* **534** (2004) 269 [[hep-ph/0405098](https://arxiv.org/abs/hep-ph/0405098)].
- [4] F. Yuasa, E. de Doncker, N. Hamaguchi, T. Ishikawa, K. Kato, Y. Kurihara et al., *Numerical Computation of Two-loop Box Diagrams with Masses*, *Comput. Phys. Commun.* **183** (2012) 2136 [[1112.0637](https://arxiv.org/abs/1112.0637)].
- [5] E. de Doncker, F. Yuasa, K. Kato, T. Ishikawa, J. Kapenga and O. Olagbemi, *Regularization with Numerical Extrapolation for Finite and UV-Divergent Multi-loop Integrals*, *Comput. Phys. Commun.* **224** (2018) 164 [[1702.04904](https://arxiv.org/abs/1702.04904)].
- [6] J. Baglio, F. Campanario, S. Glaus, M. Mühlleitner, J. Ronca, M. Spira et al., *Higgs-Pair Production via Gluon Fusion at Hadron Colliders: NLO QCD Corrections*, *JHEP* **04** (2020) 181 [[2003.03227](https://arxiv.org/abs/2003.03227)].
- [7] E. de Doncker, T. Ishikawa, K. Kato and F. Yuasa, *Analytic and Numerical Approaches for Depictive 3-Loop Integrals Using Sector Decomposition*, *PTEP* **2024** (2024) 083B08 [[2405.13286](https://arxiv.org/abs/2405.13286)].
- [8] A. Bhattacharya, F. Campanario, S. Carlotti, J. Chang, J. Mazzitelli, M. Mühlleitner et al., *Higgs-Pair Production via Gluon Fusion: Top-Yukawa- and light-quark-induced electroweak Corrections*, [2512.14823](https://arxiv.org/abs/2512.14823).
- [9] S.C. Borowka, *Evaluation of multi-loop multi-scale integrals and phenomenological two-loop applications*, Ph.D. thesis, Munich, Tech. U., 2014. [1410.7939](https://arxiv.org/abs/1410.7939).

[10] S. Borowka, G. Heinrich, S.P. Jones, M. Kerner, J. Schlenk and T. Zirke, *SecDec-3.0: Numerical evaluation of multi-scale integrals beyond one loop*, *Comput. Phys. Commun.* **196** (2015) 470 [[1502.06595](#)].

[11] S. Borowka, G. Heinrich, S. Jahn, S.P. Jones, M. Kerner, J. Schlenk et al., *pySecDec: A toolbox for the numerical evaluation of multi-scale integrals*, *Comput. Phys. Commun.* **222** (2018) 313 [[1703.09692](#)].

[12] S. Borowka, G. Heinrich, S. Jahn, S.P. Jones, M. Kerner and J. Schlenk, *A GPU compatible quasi-Monte Carlo integrator interfaced to pySecDec*, *Comput. Phys. Commun.* **240** (2019) 120 [[1811.11720](#)].

[13] S. Jahn, *Automation of Multi-Loop Amplitude Calculations*, Ph.D. thesis, Munich, Tech. U., 2020.

[14] G. Heinrich, S. Jahn, S.P. Jones, M. Kerner, F. Langer, V. Magerya et al., *Expansion by regions with pySecDec*, *Comput. Phys. Commun.* **273** (2022) 108267 [[2108.10807](#)].

[15] G. Heinrich, S.P. Jones, M. Kerner, V. Magerya, A. Olsson and J. Schlenk, *Numerical scattering amplitudes with pySecDec*, *Comput. Phys. Commun.* **295** (2024) 108956 [[2305.19768](#)].

[16] A.V. Smirnov, *FIESTA 3: cluster-parallelizable multiloop numerical calculations in physical regions*, *Comput. Phys. Commun.* **185** (2014) 2090 [[1312.3186](#)].

[17] A.V. Smirnov, *FIESTA4: Optimized Feynman integral calculations with GPU support*, *Comput. Phys. Commun.* **204** (2016) 189 [[1511.03614](#)].

[18] A.V. Smirnov, N.D. Shapurov and L.I. Vysotsky, *FIESTA5: Numerical high-performance Feynman integral evaluation*, *Comput. Phys. Commun.* **277** (2022) 108386 [[2110.11660](#)].

[19] M. Borinsky, H.J. Munch and F. Tellander, *Tropical Feynman integration in the Minkowski regime*, *Comput. Phys. Commun.* **292** (2023) 108874 [[2302.08955](#)].

[20] D.E. Soper, *QCD calculations by numerical integration*, *Phys. Rev. Lett.* **81** (1998) 2638 [[hep-ph/9804454](#)].

[21] D.E. Soper, *Techniques for QCD calculations by numerical integration*, *Phys. Rev. D* **62** (2000) 014009 [[hep-ph/9910292](#)].

[22] T. Binoth, J.P. Guillet, G. Heinrich, E. Pilon and C. Schubert, *An Algebraic/numerical formalism for one-loop multi-leg amplitudes*, *JHEP* **10** (2005) 015 [[hep-ph/0504267](#)].

[23] Z. Nagy and D.E. Soper, *Numerical integration of one-loop Feynman diagrams for N-photon amplitudes*, *Phys. Rev. D* **74** (2006) 093006 [[hep-ph/0610028](#)].

[24] C. Anastasiou, S. Beerli, S. Bucherer, A. Daleo and Z. Kunszt, *Two-loop amplitudes and master integrals for the production of a Higgs boson via a massive quark and a scalar-quark loop*, *JHEP* **01** (2007) 082 [[hep-ph/0611236](#)].

[25] C. Anastasiou, S. Beerli and A. Daleo, *Evaluating multi-loop Feynman diagrams with infrared and threshold singularities numerically*, *JHEP* **05** (2007) 071 [[hep-ph/0703282](#)].

[26] A. Lazopoulos, K. Melnikov and F. Petriello, *QCD corrections to tri-boson production*, *Phys. Rev. D* **76** (2007) 014001 [[hep-ph/0703273](#)].

[27] A. Lazopoulos, K. Melnikov and F.J. Petriello, *NLO QCD corrections to the production of $t\bar{t}Z$ in gluon fusion*, *Phys. Rev. D* **77** (2008) 034021 [[0709.4044](#)].

[28] C. Anastasiou, S. Beerli and A. Daleo, *The Two-loop QCD amplitude $gg \rightarrow h, H$ in the Minimal Supersymmetric Standard Model*, *Phys. Rev. Lett.* **100** (2008) 241806 [[0803.3065](#)].

[29] W. Gong, Z. Nagy and D.E. Soper, *Direct numerical integration of one-loop Feynman diagrams for N -photon amplitudes*, *Phys. Rev. D* **79** (2009) 033005 [[0812.3686](#)].

[30] S. Becker, C. Reuschle and S. Weinzierl, *Numerical NLO QCD calculations*, *JHEP* **12** (2010) 013 [[1010.4187](#)].

[31] S. Mizera and S. Telen, *Landau discriminants*, *JHEP* **08** (2022) 200 [[2109.08036](#)].

[32] E. Gardi, F. Herzog, S. Jones and Y. Ma, *Dissecting polytopes: Landau singularities and asymptotic expansions in $2 \rightarrow 2$ scattering*, *JHEP* **08** (2024) 127 [[2407.13738](#)].

[33] R. Winterhalder, V. Magerya, E. Villa, S.P. Jones, M. Kerner, A. Butter et al., *Targeting multi-loop integrals with neural networks*, *SciPost Phys.* **12** (2022) 129 [[2112.09145](#)].

[34] T. Binoth and G. Heinrich, *An automatized algorithm to compute infrared divergent multi-loop integrals*, *Nucl. Phys. B* **585** (2000) 741 [[hep-ph/0004013](#)].

[35] T. Janßen, R. Poncelet and S. Schumann, *Sampling NNLO QCD phase space with normalizing flows*, *JHEP* **09** (2025) 194 [[2505.13608](#)].

[36] E. Bothmann, T. Janßen, M. Knobbe, T. Schmale and S. Schumann, *Exploring phase space with Neural Importance Sampling*, *SciPost Phys.* **8** (2020) 069 [[2001.05478](#)].

[37] C. Gao, S. Höche, J. Isaacson, C. Krause and H. Schulz, *Event Generation with Normalizing Flows*, *Phys. Rev. D* **101** (2020) 076002 [[2001.10028](#)].

[38] T. Heimel, R. Winterhalder, A. Butter, J. Isaacson, C. Krause, F. Maltoni et al., *MadNIS - Neural multi-channel importance sampling*, *SciPost Phys.* **15** (2023) 141 [[2212.06172](#)].

[39] C. Gao, J. Isaacson and C. Krause, *i-flow: High-dimensional Integration and Sampling with Normalizing Flows*, *Mach. Learn. Sci. Tech.* **1** (2020) 045023 [[2001.05486](#)].

[40] J. Bendavid, *Efficient Monte Carlo Integration Using Boosted Decision Trees and Generative Deep Neural Networks*, [1707.00028](#).

[41] M.D. Klimek and M. Perelstein, *Neural Network-Based Approach to Phase Space Integration*, *SciPost Phys.* **9** (2020) 053 [[1810.11509](#)].

[42] F. Bishara and M. Montull, *Machine learning amplitudes for faster event generation*, *Phys. Rev. D* **107** (2023) L071901 [[1912.11055](#)].

[43] S. Otten, S. Caron, W. de Swart, M. van Beekveld, L. Hendriks, C. van Leeuwen et al., *Event Generation and Statistical Sampling for Physics with Deep Generative Models and a Density Information Buffer*, *Nature Commun.* **12** (2021) 2985 [[1901.00875](#)].

[44] E. Bothmann, T. Janßen, M. Knobbe, B. Schmitzer and F. Sinz, *Efficient many-jet event generation with Flow Matching*, [2506.18987](#).

[45] R. Jinno, G. Kälin, Z. Liu and H. Rubira, *Machine learning Post-Minkowskian integrals*, *JHEP* **07** (2023) 181 [[2209.01091](#)].

[46] D. Maître and R. Santos-Mateos, *Multi-variable integration with a neural network*, *JHEP* **03** (2023) 221 [[2211.02834](#)].

[47] J. Dick, F.Y. Kuo and I.H. Sloan, *High-dimensional integration: The quasi-monte carlo way*, *Acta Numerica* **22** (2013) 133–288.

- [48] T. Goda and P. L'Ecuyer, *Construction-free median quasi-monte carlo rules for function spaces with unspecified smoothness and general weights*, *SIAM Journal on Scientific Computing* **44** (2022) A2765–A2788.
- [49] C. Bogner and S. Weinzierl, *Resolution of singularities for multi-loop integrals*, *Comput. Phys. Commun.* **178** (2008) 596 [[0709.4092](#)].
- [50] A.V. Smirnov and V.A. Smirnov, *Hepp and Speer Sectors within Modern Strategies of Sector Decomposition*, *JHEP* **05** (2009) 004 [[0812.4700](#)].
- [51] T. Kaneko and T. Ueda, *A Geometric method of sector decomposition*, *Comput. Phys. Commun.* **181** (2010) 1352 [[0908.2897](#)].
- [52] T. Kaneko and T. Ueda, *Sector Decomposition Via Computational Geometry*, *PoS ACAT2010* (2010) 082 [[1004.5490](#)].
- [53] J.K. Schlenk, *Techniques for higher order corrections and their application to LHC phenomenology*, Ph.D. thesis, Munich, Tech. U., 8, 2016.
- [54] D. Hendrycks and K. Gimpel, *Gaussian error linear units (gelus)*, 2023.
- [55] Z. Pan, *Automatic optimal-rate convergence of randomized nets using median-of-means*, 2025.
- [56] A.B. Owen, *Error estimation for quasi-monte carlo*, 2025.

A Analytical threshold derivation

In this section, we derive an analytic formula for the p_4^2 dependence of the s threshold for the integrand of Section 6.3. We start from the F polynomial

$$\begin{aligned} F = & m^2 (x_2 x_5 + x_1 x_5 + x_3 + x_4 x_5 + 1) \\ & \times (x_2 x_3 + x_2 x_5 + x_2 + x_1 x_3 + x_1 x_5 + x_1 + x_3 x_4 + x_3 + x_4 x_5 + x_4 + 1) \\ & - p_4^2 (x_2 x_3 + x_1 x_3 + x_1 x_5 + x_3 x_4 + x_3) \\ & - s x_2 x_5 (x_1 x_3 + x_1 x_5 + x_1 + x_3) - t x_4 x_5 \end{aligned} \quad (\text{A.1})$$

and substitute $m^2 = 1$, $t = -(s - p_4^2)\tau$ and $p_4^2 = \gamma s$. Using the numerical minimisation described in Section 6, we observe that the minimum always occurs for $x_1 = 1$, $x_2 = 1$, $x_4 = 0$ and $x_5 = 1$, leaving us with,

$$F = -s(\gamma + (3\gamma + 2)x_3 + 2) + 3x_3^2 + 14x_3 + 15. \quad (\text{A.2})$$

We now solve $F = 0$ for s to obtain

$$s = \frac{3x_3^2 + 14x_3 + 15}{\gamma + 3\gamma x_3 + 2x_3 + 2}, \quad (\text{A.3})$$

the minimum value for s is obtained for

$$x_3 = \frac{4\sqrt{3}\sqrt{6\gamma^2 + 5\gamma + 1} - 3\gamma - 6}{3(3\gamma + 2)}. \quad (\text{A.4})$$

Inserting back into Eq. (A.3) and simplifying yields

$$s = \frac{4(9\gamma + 2\sqrt{3\gamma(6\gamma + 5) + 3} + 4)}{(3\gamma + 2)^2}. \quad (\text{A.5})$$

This expression evaluates to $4 + 2\sqrt{3} \approx 7.46$ in the limit of vanishing p_4^2 and reverts to the physical threshold location $s = 4$ in the limit $p_4^2 \rightarrow s$.

B Comparison of λ_i values

Figure 21 and Figure 22 show a comparison of the values of λ_i chosen by pySECDEC and those chosen by the $\lambda(\mathbf{s})$ networks.

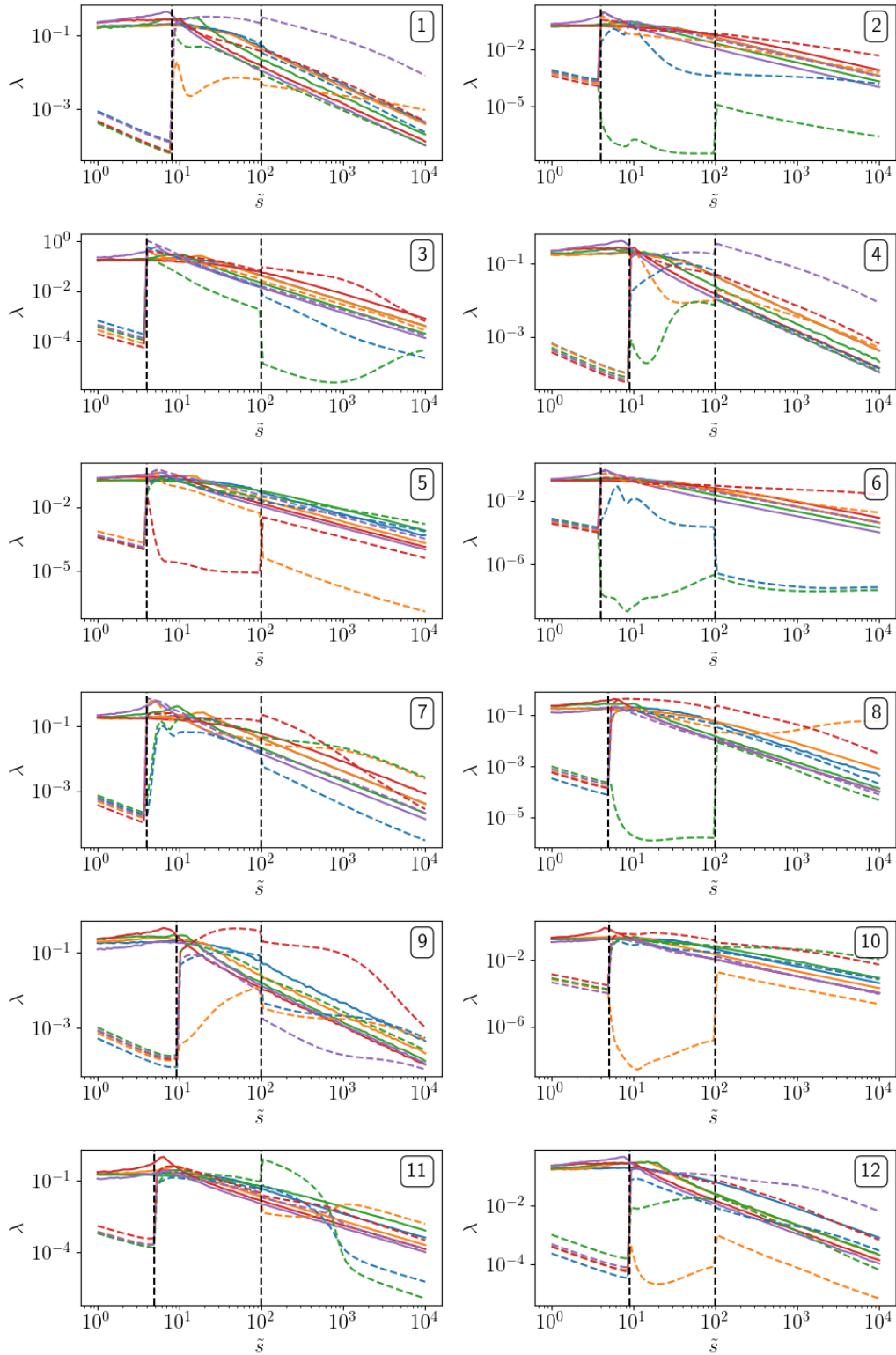


Figure 21. Comparison between the λ values for pySECDEC (solid) and the NN-guided values (dashed). Curves of the same colour correspond to the deformation strength for the same coordinate. The sector number is displayed in the upper right of each plot. The vertical dashed lines show the separation between different trainings, where discontinuities can be expected.

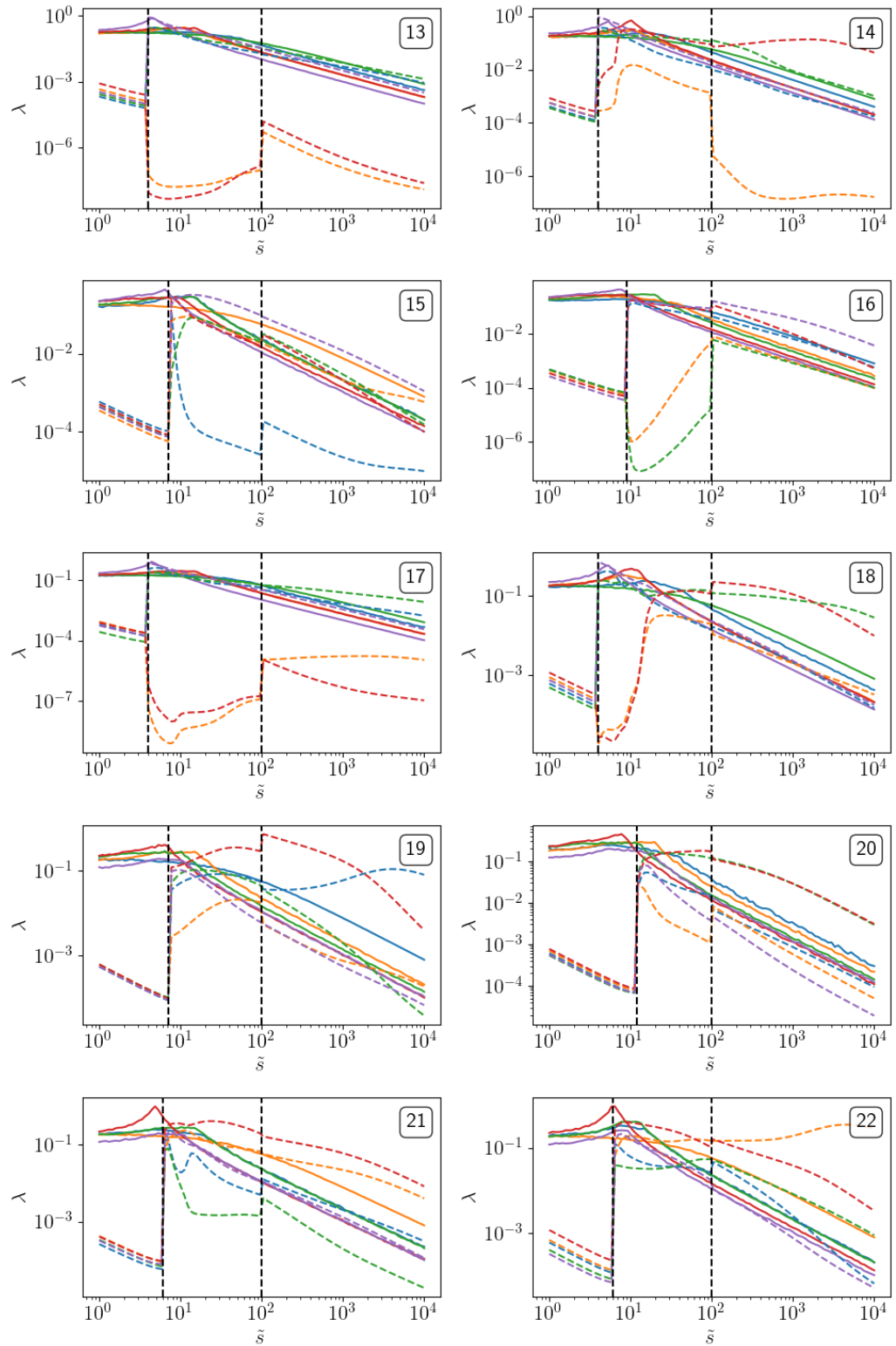


Figure 22. Comparison between the λ values for pySECDEC (solid) and the NN-guided values (dashed). Curves of the same colour correspond to the deformation strength for the same coordinate. The sector number is displayed in the upper right of each plot. The vertical dashed lines show the separation between different trainings, where discontinuities can be expected.